JCB Journal of Cell Biology

ARTICLE

Septin-coated microtubules promote maturation of multivesicular bodies by inhibiting their motility

Benjamin P. Robinson[1], Naomi R. Bass[1], Priyanka Bhakt[1], and Elias T. Spiliotis[1,2]

The microtubule cytoskeleton consists of microtubule subsets with distinct compositions of microtubule-associated proteins, which instruct the position and traffic of subcellular organelles. In the endocytic pathway, these microtubule-associated cues are poorly understood. Here, we report that in MDCK cells, endosomes with multivesicular body (MVB) and late endosome (LE) markers localize preferentially to microtubules coated with septin GTPases. Compared with early endosomes, CD63-containing MVBs/LEs are largely immotile on septin-coated microtubules. In vitro reconstitution assays revealed that the motility of isolated GFP-CD63 endosomes is directly inhibited by microtubule-associated septins. Quantification of CD63-positive endosomes containing the early endosome antigen (EEA1), the Rab7 effector and dynein adaptor RILP or Rab27a, showed that intermediary EEA1- and RILP-positive GFP-CD63 preferentially associate with septin-coated microtubules. Septin knockdown enhanced GFP-CD63 motility and decreased the percentage of CD63-positive MVBs/LEs with lysobiphosphatidic acid without impacting the fraction of EEA1-positive CD63. These results suggest that MVB maturation involves immobilization on septin-coated microtubules, which may facilitate multivesiculation and/or organelle–organelle contacts.

Introduction

In the microtubule network, organelle positioning and movement takes place on microtubules with distinct compositions of tubulin isotypes, posttranslational modifications (PTMs), and microtubule-associated proteins (Atherton et al., 2013; Balabanian et al., 2018; Barlan and Gelfand, 2017; Bodakuntla et al., 2019; Park and Roll-Mecak, 2018). The biochemical heterogeneity of microtubules provides a code for the spatial organization and traffic of membrane organelles and vesicles (Barlan and Gelfand, 2017; Bodakuntla et al., 2019; Magiera and Janke, 2014; Park and Roll-Mecak, 2018). Organelles such as the ER and lysosomes associate with polyglutamylated and detyrosinated microtubules, respectively, which facilitate the position of perinuclear ER and lysosome fusion with autophagosomes (Mohan et al., 2019; Zheng et al., 2022). In the endocytic pathway, lysosomes driven by different kinesin motors traffic on microtubule tracks of distinct PTMs (Guardia et al., 2016). However, the microtubule-associated cues and mechanisms that underlie the traffic and position of endolysosomes are largely unknown. Uncovering these microtubule-based cues is critical for understanding the biogenesis of endosomal organelles, which occurs concomitantly with their intracellular movement (Huotari and Helenius, 2011; Jongsma et al., 2023; Klumperman and Raposo, 2014; Winckler et al., 2018).

Multivesicular bodies (MVBs) are endocytic organelles that arise from early endosomes and contain multiple intralumenal vesicles (ILVs) (Hanson and Cashikar, 2012; Huotari and Helenius, 2011; Piper and Katzmann, 2007). MVBs sort and internalize proteins destined for degradation in the lysosome or secretion from the plasma membrane in ILVs termed exosomes (Hanson and Cashikar, 2012; Klumperman and Raposo, 2014; Raposo and Stoorvogel, 2013). Owing to their degradative and exocytic functions, MVBs are physiologically important for protein homeostasis, cell signaling, autophagy, adaptive and innate immunity, and intercellular communication (Bobrie et al., 2011; Fader and Colombo, 2009; Katzmann et al., 2002; Raposo and Stoorvogel, 2013; von Zastrow and Sorkin, 2021; Ye et al., 2018).

The biogenesis of MVBs begins with the formation of ILVs by components of the endosomal sorting complex required for transport (ESCRT) machinery, which sorts and packages ubiquitinated proteins into ILVs (Babst, 2011; Hanson and Cashikar, 2012; Henne et al., 2011, 2013). Inward budding of ILVs is aided by lipids such as lysobisphosphatidic acid (LBPA), cholesterol,

[1]Department of Biology, Drexel University, Philadelphia, PA, USA; [2]Department of Cell Biology, University of Virginia School of Medicine, Charlottesville, VA, USA.

Correspondence to Elias T. Spiliotis: dkg4jc@virginia.edu

P. Bhakt's current affiliation is Department of Pathology and Laboratory Medicine, University of Pennsylvania, Perelman School of Medicine, Philadelphia, PA, USA.

and ceramide, which can modulate membrane curvature and stiffness (Alonso and Goni, 2018; Doole et al., 2023; Gruenberg, 2020). MVB maturation is marked by Rab GTPase switching and an acidification of the lumenal pH (<6.0) by the vacuolar H^+-ATPase (Chadwick et al., 2021; Clague and Urbe, 2008; Clague et al., 1994; Falguieres et al., 2008; Shi et al., 2022). A Rab5-to-Rab7 switch induces retrograde movement by recruiting the Rab7-interacting lysosomal protein (RILP), an adaptor of dynein–dynactin motor complex (Bonifacino and Neefjes, 2017; Cantalupo et al., 2001; Jongsma et al., 2023; Poteryaev et al., 2010; Rink et al., 2005). Conversely, a Rab7-to-Arl8b transition enables recruitment of kinesin motors and the anterograde movement of MVBs for fusion with the plasma membrane, which is further enabled by Arl8-to-Rab27a conversion (Jongsma et al., 2020; Keren-Kaplan and Bonifacino, 2021; Verweij et al., 2022).

How MVB maturation to endolysosomal or exosomal compartments is spatially coupled to the underlying microtubule cytoskeleton is poorly understood. Lysosomes with an acidic luminal pH localize to the perinuclear center, and centripetal movement is considered a hallmark of early to late endosome (LE) maturation (Collinet et al., 2010; Huotari and Helenius, 2011; Johnson et al., 2016). Perinuclear localization of MVBs, however, can also expedite fusion with the plasma membrane, and therefore, it is not a distinguishing factor between MVBs that mature into endolysosomes and MVBs destined for exocytosis (Verweij et al., 2022). This raises the question of how MVB maturation and microtubule motor-driven movement are spatially coordinated with the degradative and exocytic routes to endolysosomes and the plasma membrane, respectively.

Septins are GTP-binding proteins that assemble into higher-order oligomers and polymers (Cavini et al., 2021; Mostowy and Cossart, 2012; Woods and Gladfelter, 2021). Septins associate with subsets of actin filaments and microtubules, and membrane subdomains (Benoit et al., 2023; Cannon et al., 2017; Spiliotis and Nakos, 2021). Growing evidence indicates that septins function at the interface of the cytoskeleton and endolysosomal membranes in regulating endocytic trafficking (Dolat and Spiliotis, 2016; Krokowski et al., 2018; Song et al., 2016). Endosomal adaptor proteins (AP3, SNX21) and ESCRTs (TSG101) interact with septins, and the maturation of macropinosomes and MVBs is impaired by septin depletion (Baust et al., 2008; Danson et al., 2018; Dolat and Spiliotis, 2016; Karasmanis et al., 2019; O'Loughlin et al., 2018). On endosomal membranes, septins can promote the retrograde dynein-mediated transport of lysosomes and the homotypic fusion of macropinosomes (Kesisova et al., 2021). However, septins also impact the organization of actin filaments that underlie the movement of early endosomes, which is critical for endosomal enrichment with stage-specific sorting proteins and cargo (O'Loughlin et al., 2018; Traikov et al., 2014).

In epithelial and neuronal cells, septins associate with subsets of microtubules regulating vesicular traffic by modulating the motility of kinesin and dynein motors (Bai et al., 2013; Bowen et al., 2011; Froidevaux-Klipfel et al., 2011; Hu et al., 2012; Karasmanis et al., 2018; Spiliotis et al., 2005, 2008; Targa et al., 2019). Microtubule-associated septin complexes regulate microtubule motor motility with differential specificities, and might be part of the microtubule-associated codes that spatially control membrane traffic (Kesisova et al., 2021; Suber et al., 2023). Here, we analyzed the subcellular distribution of endosomal organelles with respect to the septin-coated microtubules in Madin–Darby canine kidney (MDCK) epithelia. We found that endosomes with MVB and LE marker proteins associate preferentially with septin-coated microtubules, which in turn promote the maturation MVBs by restricting intracellular motility.

Results

Endosomes with the MVB/LE markers TSG101, LBPA, and CD63 localize preferentially to septin-coated microtubules

We sought to analyze the subcellular distribution of endosomal compartments with respect to subsets of microtubules, which are coated with septins. We performed this analysis in subconfluent monolayers of MDCK cells, where septins localize to subsets of microtubules (Bai et al., 2013; Bowen et al., 2011; Spiliotis et al., 2008). In agreement with previous studies, endogenous septins (SEPT7, SEPT9) were enriched on a microtubule subpopulation that included perinuclear microtubule bundles (Fig. 1 A) (Bowen et al., 2011). This was not an artifact of fixation and/or extraction. In an MDCK cell line that stably expressed mCherry-SEPT9_i1 at endogenous levels (Dolat et al., 2014), mCherry-SEPT9_i1 localized to subsets of microtubules labeled with α-tubulin-GFP and antibody against α-tubulin (Fig. S1). The septin-coated subset of microtubules is primarily polyglutamylated (Spiliotis et al., 2008) and tyrosinated (Fig. S2 A), which is consistent with previous work indicating that these PTMs promote septin recruitment to microtubules (Froidevaux-Klipfel et al., 2015). Staining for detyrosinated and acetylated microtubules showed partial colocalization with septins; septin-coated segments had low levels of detyrosinated and acetylated tubulin (Fig. S2, B and C). In MDCK cells, SEPT7 and SEPT9 colocalize with SEPT2 and SEPT6 (Dolat et al., 2014), and thus microtubule-associated septins most likely consist of SEPT2/6/7/9 complexes that have been shown to directly bind microtubules in vitro (Kuzmic et al., 2022; Suber et al., 2023). In this study, we used SEPT7 and SEPT9 interchangeably as markers of septin-coated microtubules, which are also referred to as septin filaments owing to the filamentous appearance of microtubule-associated septins.

To distinguish between early and late endosomal compartments, we stained MDCK cells with antibodies against the early endosome antigen 1 (EEA1) and LAMTOR4, which is an LE/lysosome marker protein (Fig. 1, B and C). Quantification of the subcellular distribution of EEA1- and LAMTOR4-positive compartments revealed that a higher percentage of LEs (53%) overlaps with septin filaments than early endosomes (35%) (Fig. 1 G). We also analyzed the distribution of endosomes that were positive for the ESCRT-I protein TSG101 and the lipid LBPA, which promotes the formation of the ILVs of MVBs (Matsuo et al., 2004). The percentage of TSG101- and LBPA-containing compartments that localized to septin filaments was 63% (Fig. 1, D, E, and G). To further corroborate whether this

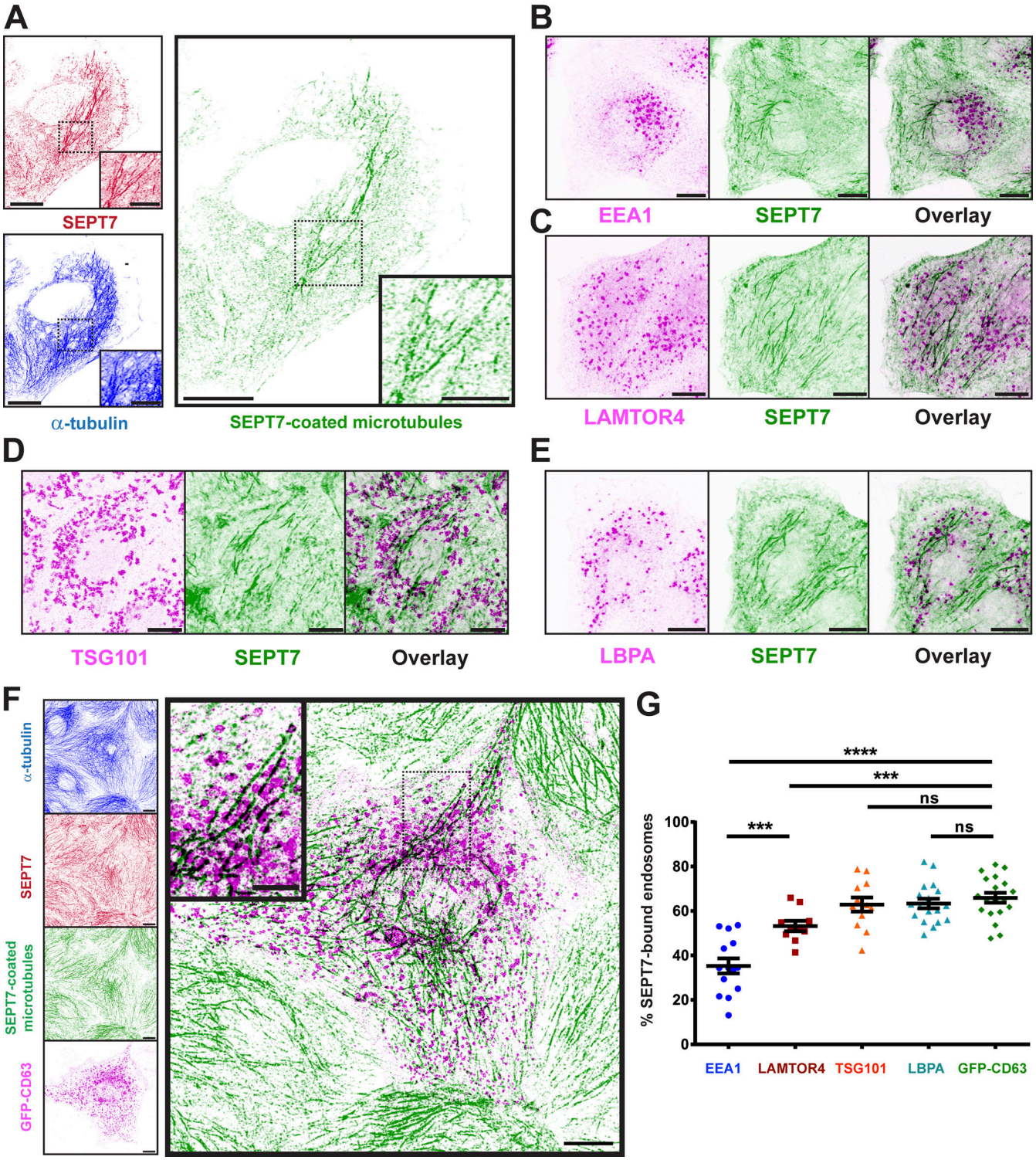

Figure 1. **MVBs/LEs associate preferentially with septin-coated microtubules. (A)** Super-resolution confocal microscopy images of an MDCK cell stained for endogenous SEPT7 (inverted burgundy) and α-tubulin (inverted blue). The microtubule subset that colocalizes with SEPT7 is shown as an individual fluorescent channel (SEPT7-coated microtubules; inverted forest green). Insets show in higher magnification the perinuclear regions outlined with a dashed rectangle. Scale bar, 10 and 5 µm (insets). **(B–E)** Confocal microscopy images show single optical sections from subconfluent monolayers of MDCK cells stained with antibodies against SEPT7 and EEA1 (B), LAMTOR4 (C), TSG101 (D), and LBPA (E). Scale bars, 10 µm. **(F)** Subconfluent monolayers of MDCK cells that stably express GFP-CD63 (inverted magenta) were stained with antibodies to SEPT7 (inverted burgundy) and α-tubulin (inverted blue). Image (right panel) shows a maximum intensity projection of GFP-CD63 (inverted magenta) and the subset of microtubules that colocalizes with SEPT7 (SEPT7-coated microtubules; inverted forest green) from a z-series stack of optical sections acquired with super-resolution microscopy. Scale bars, 10 and 5 µm (inset). **(G)** Quantification of the mean (±SEM, error bars) percentage of EEA1 (n = 14 cells), LAMTOR4 (n = 10 cells), TSG101 (n = 12 cells), LBPA (n = 18 cells), and GFP-CD63 (n = 19 cells) membranes that overlap with septin filaments per MDCK cell. Statistical analysis of pairwise comparisons was performed with an unpaired t test with Welch's correction. n.s., not significant; *** $P < 0.001$, **** $P < 0.0001$.

is an MVB-related endosome population with higher levels of association with septin filaments, we generated a stable MDCK cell line with low levels of GFP-CD63 expression as CD63 antibodies did not work in MDCK cells; CD63 is a tetraspanin protein that is enriched in the ILVs of MVBs (Andreu and Yanez-Mo, 2014; Pols and Klumperman, 2009; van Niel et al., 2011). We found that 66% of GFP-CD63–containing compartments localized to septin filaments (Fig. 1, F and G). Overall, there were 2- and 1.5-fold more endosomes with MVB and lysosomal markers, respectively, localizing to septin filaments than early endosomes. This spatial bias was not due to a higher percentage of perinuclear LEs relative to early endosomes as LBPA-, LAMTOR4-, and EEA1-containing endosomes all had a similar percentage (34 ± 3%; n = 6–9 cells) of compartments localizing within a 5-µm-wide zone from the nuclear envelope. The percentage of GFP-CD63 compartments that overlapped with SEPT7-coated microtubules (74 ± 2%, n = 6 cells), which were generated artificially through fluorescence mask subtraction (Fig. 1 F), was similar to that of the whole SEPT7. In contrast, only 23 ± 3.5% (n = 9 cells) of GFP-CD63 overlapped with SEPT7-coated actin filaments which localized predominately to the periphery of GFP-CD63 (Fig. S3). Taken together, these data indicate that MVBs/LEs localize preferentially to septin-bound microtubules.

CD63-containing endosomes are less motile than early EEA1-positive endosomes on septin-coated microtubules

We set out to determine the dynamics of the endosomes that overlap with septin filaments that coalign with microtubules and how they compare to endosomes that do not overlap with these microtubule-associated septins. Using time-lapse super-resolution spinning disk confocal microscopy, we first imaged MDCK-mCherry-SEPT9_i1 cells expressing GFP-CD63, which has the highest percentage of septin-bound compartments. GFP-CD63-containing endosomes were largely stationary on septin-coated microtubules (Fig. 2 A, orange arrows; and Video 1). On occasions, GFP-CD63 underwent short-range movements, switching between neighboring septin filaments (Fig. 2 B, orange arrows; and Video 2). On septin filaments, CD63-GFP endosomes exhibited repeated organelle–organelle contacts, merging transiently and disengaging subsequently into two distinct compartments (Fig. 2 C, arrows). Processive movement along a septin filament was rare, but occurred occasionally (Fig. 2 D and Video 3).

We quantified stationary and motile GFP-CD63 endosomes by analyzing their displacement between successive frames; particles with center of mass displacements of <500 nm were deemed as stationary. Strikingly, only 16% of septin-bound GFP-CD63 endosomes were motile on mCherry-SEPT9_i1 (Fig. 2 E). Quantification of the motile events of septin-bound GFP-CD63 showed that ∼40% of the movements were unidirectional and the rest were either bidirectional or diffusive with the latter being a little more abundant than the former (Fig. 2 F). In contrast to the low percentage of motile SEPT9-bound GFP-CD63, 73% of SEPT9-free GFP-CD63 endosomes were motile (Fig. 2 E). Thus, GFP-CD63 endosomes appear to immobilize on septin-coated microtubules, which increases the percentage of stationary GFP-CD63 by more than fourfold.

Next, we analyzed the motility of early endosomes with GFP-EEA1 (Fig. 2 G). Despite EEA1 having the lowest percentage of association with septin-coated microtubules, the percentage of GFP-EEA1 that overlapped with microtubules (95.6 ± 0.7%; n = 6 cells) was similar to that of GFP-CD63 (98.9 ± 0.4%, n = 8 cells), and GFP-EEA1 was more motile than GFP-CD63. We found that 51% of total septin-bound GFP-EEA1 endosomes were motile, which was over threefold more than GFP-CD63 (Fig. 2 G). Notably, this percentage was slightly higher than the percentage (46%) of motile GFP-EEA1 that did not associate with mCherry-SEPT9_i1. Therefore, septin-bound GFP-EEA1 endosomes are at least as motile as their unbound counterparts, which is in striking contrast with the immobilization of GFP-CD63 on mCherry-SEPT9_i1. These data indicate that the motility of GFP-CD63 endosomes is selectively arrested on septin-coated microtubules.

Microtubule-associated septins directly inhibit the motility of isolated GFP-CD63 endosomes in cell-free in vitro reconstitution assays

We next sought to test whether microtubule-associated septins directly inhibit the motility of GFP-CD63 endosomes. We set up an in vitro reconstitution assay of GFP-CD63 motility using total internal reflection fluorescence (TIRF) microscopy, recombinant septin complexes, which were purified from bacteria, and GFP-CD63 endosomes that were isolated from MDCK cells by differential centrifugation. As a proof of principle, we first reconstituted GFP-CD63 motility on taxol-stabilized microtubules in the absence of septins. GFP-CD63 endosomes were motile and underwent processive movements with velocity (0.32 ± 0.028 µm/s; n = 68), which approximated the velocity of their intracellular movement (0.43 ± 0.002 µm/s; n = 2,640) (Fig. 3 A and Video 4). The percentage of GFP-CD63 endosomes with processive movement (19.7 ± 0.03%) was similar to previous reconstitutions of the motility of endosomes isolated from whole tissues (Hendricks et al., 2010).

To examine how septin complexes impact the microtubule association and motility of GFP-CD63 endosomes, we expressed in bacteria and purified septin complexes consisting of mCherry-tagged SEPT2/6/7 and SEPT2/6/7/9 as we recently performed for in vitro single molecule assays of kinesin and dynein motility (Suber et al., 2023). We also purified the microtubule-binding domain of MAP4, mCherry-MAP4(654–1090), as a control bona fide microtubule-associated protein (MAP). On microtubules decorated with mCherry-SEPT2/6/7, the percentage of motile GFP-CD63 particles was reduced from 19.7 to 6.9% (n = 13–33 microtubules; 43–63 particles, P = 0.008), and the percentage of motile GFP-CD63 that paused increased from 28 ± 10 to 68 ± 23% (P < 0.05) with approximately three-quarters of the latter taking place at microtubule segments with mCherry-SEPT2/6/7 (Fig. 3 B and Video 5). GFP-CD63 motility, however, was more drastically impaired by microtubule-associated mCherry-SEPT2/6/7/9, which immobilized them in place (Fig. 3 C and Video 6). GFP-CD63 exhibited no processive motility on microtubules decorated with mCherry-SEPT2/6/7/9 (Fig. 3, C, E, and F). This effect was consistent with results from kinesin and

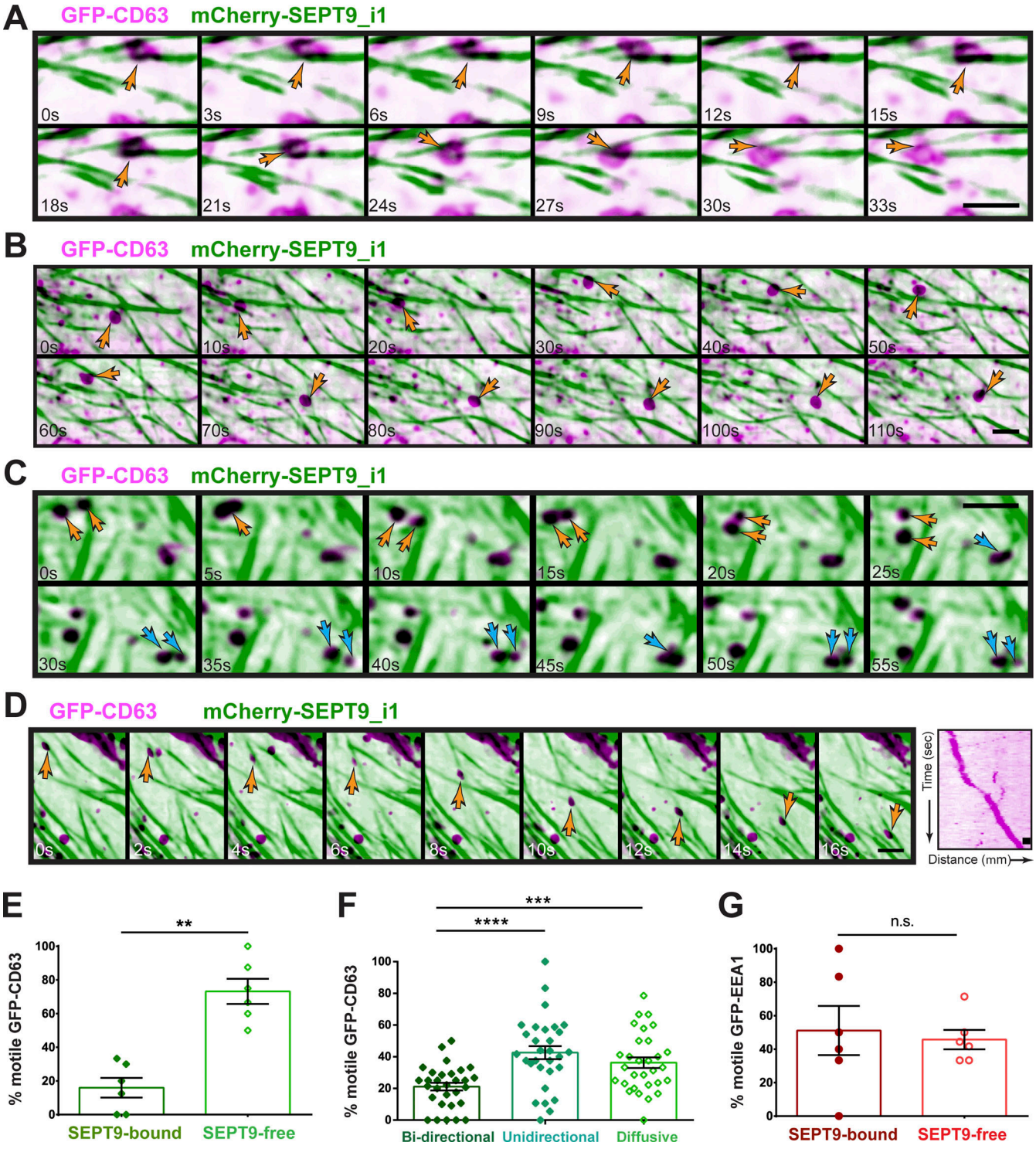

Figure 2. **CD63-containing endosomes are less motile on septin-coated microtubules than EEA1-positive endosomes. (A and B)** Still frames from time-lapse super-resolution spinning disk confocal microscopy of MDCK cells that express mCherry-SEPT9_i1 and GFP-CD63 show examples of septin-bound endosomes that are immotile (A, orange arrows) and shift between septin filaments (B, orange arrows). See also Videos 1 and 2. Scale bars, 1 µm. **(C and D)** Still frames from time-lapse super-resolution spinning disk confocal microscopy of MDCK cells that express mCherry-SEPT9_i1 and GFP-CD63 show examples of septin-bound endosomes, which transiently merge and disengage in a touch-and-go-like fashion (C, orange arrows and blue arrows), and a GFP-CD63 endosome that undergoes processive movement (D, orange arrow; see also Video 3). A kymograph illustrates the septin-bound track of the processive GFP-CD63 endosome. Scale bars, 1 µm. **(E)** Quantification of the mean percentage (±SEM, error bars) of motile GFP-CD63 endosomes with overlap with mCherry-SEPT9_i1 (SEPT9-bound) and without overlap (unbound) in subconfluent MDCK cells (n = 6). Statistical analysis of pairwise comparisons was performed with an unpaired t test with Welch's correction. ** $P < 0.01$. **(F)** Quantification of the mean percentage (±SEM, error bars) of motile septin-bound GFP-CD63 endosomes that undergo bidirectional, unidirectional, and diffusive movements on septin-coated microtubules (n = 30). Data were statistically analyzed with a Mann-Whitney test. *** $P < 0.001$; **** $P < 0.0001$. **(G)** Quantification of the mean percentage (±SEM, error bars) of motile GFP-EEA1 endosomes with overlap with mCherry-SEPT9_i1 (SEPT9-bound) and without overlap (unbound) in subconfluent MDCK cells (n = 6). Data were statistically analyzed with a Mann-Whitney test. n.s., not significant.

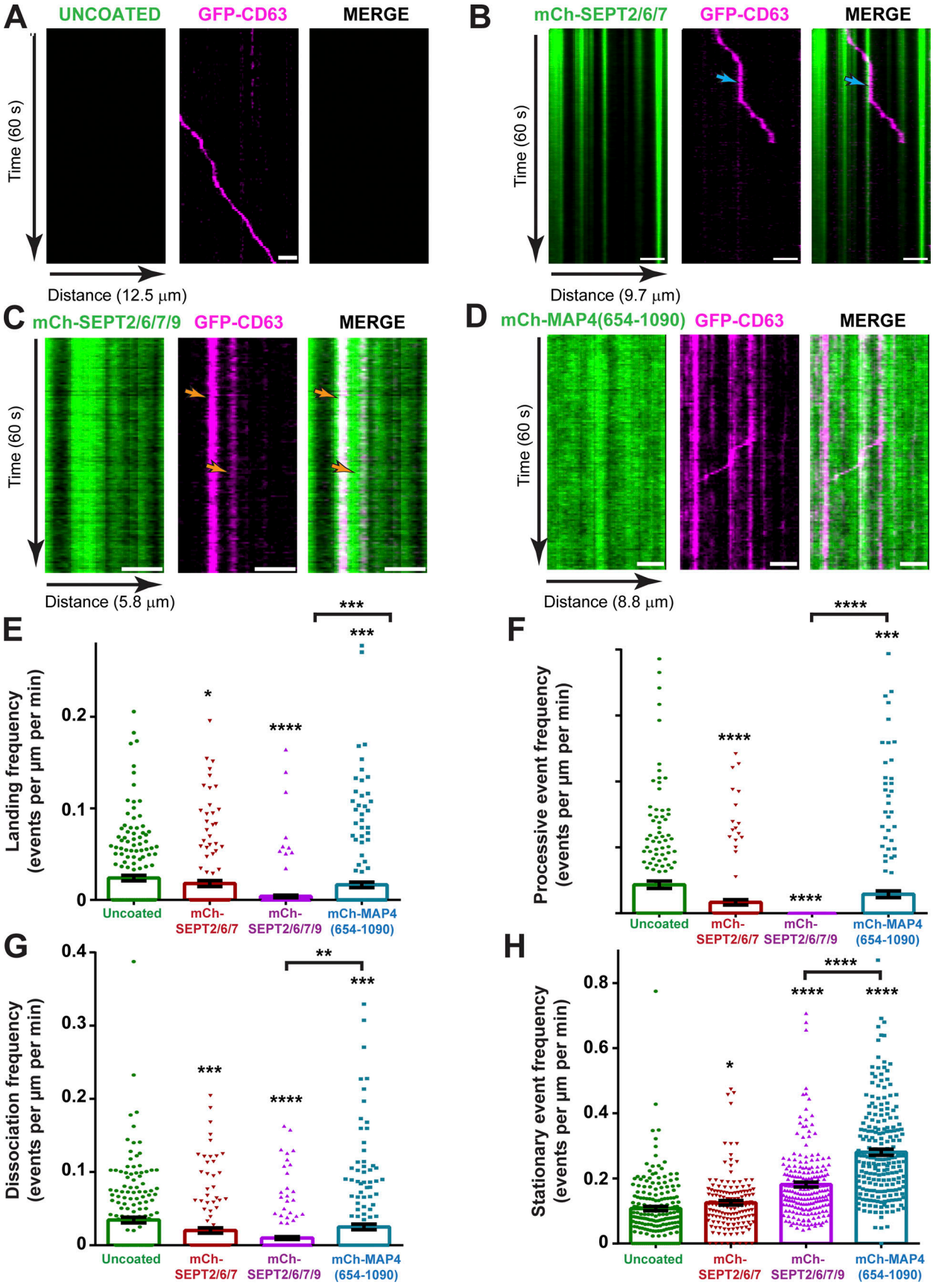

Figure 3. **Microtubule-associated septins inhibit the motility of GFP-CD63–containing endosomes in cell-free in vitro assays. (A–D)** Kymographs from time-lapse TIRF microscopy movies show motile and stationary GFP-CD63-containing endosomes (magenta) on uncoated taxol-stabilized microtubules (A; see

also Video 4) and microtubules coated with recombinant mCherry-tagged SEPT2/6/7 (1.2 µM; B, see also Video 5), SEPT2/6/7/9 (100 nM; C, see also Video 6) and MAP4(654–1090) (100 nM; D) (green). The MAPs are shown in green. GFP-CD63 endosomes were isolated by differential centrifugation from subconfluent MDCK-GFP-CD63 cells. Blue arrow points to an immobilization event of GFP-CD63 at a microtubule domain with mCherry-SEPT2/6/7. Orange arrows point to stationary GFP-CD63 at microtubule-associated mCherry-SEPT2/6/7/9. Scale bars, 2 µm. **(E and F)** Quantification of the mean frequency (±SEM, error bars) of the landing (E) and processive (F) events of GFP-CD63 per µm of microtubule length per minute. Landing events were defined as the appearance of GFP-CD63 endosomes that persisted on microtubules for at least 2 s independently of motility status. Processive events were defined as any particles with diagonal trajectories in kymographs of time-lapse movies. Data were acquired from uncoated microtubules (n = 188, eight fields of view) and microtubules coated with mCherry-tagged SEPT2/6/7 (n = 149, five fields of view), SEPT2/6/7/9 (n = 205, seven fields of view) and MAP4(654–1090) (n = 218, six fields of view). Statistical analysis of pairwise comparisons was done with a Mann-Whitney test. * P < 0.05, *** P < 0.001, **** P < 0.0001. **(G and H)** Quantification of the mean frequency (±SEM, error bars) of dissociation (G) and stationary (H) events of GFP-CD63 per µm of microtubule length per minute. Dissociation events were defined as the dissociation of microtubule-bound GFP-CD63 endosomes, which were on microtubules for at least 2 s independently of motility status. Stationary events were defined as any GFP-CD63 endosomes that did not exhibit processive movement for >5 s regardless of motility status before or after the stationary phase. Data were acquired from uncoated microtubules (n = 188, eight fields of view) and microtubules coated with mCherry-tagged SEPT2/6/7 (n = 149, five fields of view), SEPT2/67/9 (n = 205, seven fields of view) and MAP4(654–1090) (n = 218, six fields of view). Statistical analysis of pairwise comparisons between them was done with a Mann-Whitney test and comparisons were with uncoated microtubules or as indicated by the horizontal bars. * P < 0.05, ** P < 0.01, *** P < 0.001, **** P < 0.0001.

dynein motility assays, which showed that SEPT2/6/7/9 is a more potent inhibitor of kinesin-1 and dynein-dynactin-BiCD2N motility than SEPT2/6/7 (Suber et al., 2023). Quantitatively, SEPT2/6/7 complexes had a subtle effect on the frequency of GFP-CD63 landing and immobilization but strongly reduced the frequency of processive movement and dissociation from microtubules (Fig. 3, E–H). The landing and dissociation frequencies of GFP-CD63 were close to zero on microtubules decorated with SEPT2/6/7/9, which also had a larger effect than SEPT2/6/7 on the frequency of dissociation events and stationary particles (Fig. 3, E–H). SEPT2/6/7/9 was also a more potent inhibitor than MAP4(654–1090), which quantitatively resembled the effects of SEPT2/6/7 (Fig. 3, E–G). However, the microtubule-binding domain of MAP4 enhanced the frequency of stationary GFP-CD63 particles more than SEPT2/6/7 and SEPT2/6/7/9 (Fig. 3 H). This was due to a higher number of GFP-CD63 particles bound to MAP4-coated microtubules prior to the start of imaging, which took place 5–10 min after flowing GFP-CD63 into the motility chamber, indicating that MAP4 is initially more permissive to GFP-CD63 binding to microtubules than septins. Collectively, these data show that microtubule-associated septin complexes function as inhibitory MAPs that directly suppress the motility of GFP-CD63 endosomes.

EEA1-positive MVBs (GFP-CD63) are more extensively bound to septin-coated microtubules than LBPA- and Rab27a-containing MVBs

The preferential association and immobilization of CD63-positive endosomes on septin-coated microtubules raised the questions of first, whether this is a distinct subset of MVB-related endosomes, and second, if immobilization is functionally important for their maturation and/or fusion with the lysosome or the plasma membrane. To interrogate the identity of septin-bound GFP-CD63 compartments, we first stained for endogenous EEA1 and LBPA as markers of early and mature endolysosomes, respectively. Analysis of EEA1-positive and EEA1-negative GFP-CD63 compartments showed that a higher fraction of EEA1-positive GFP-CD63 compartments localized to SEPT7 filaments (Fig. 4, A–C). For EEA1-positive GFP-CD63, the ratio of SEPT7-bound to SEPT7-free compartments was 4.2 to 1, while EEA1-negative GFP-CD63 had a ratio of 1.9 to 1 (Fig. 4 D). In contrast to this strong preference of EEA1-positive GFP-CD63 for septin-coated microtubules, LBPA-negative and LBPA-positive GFP-CD63 had similar percentages of SEPT7-bound endosomes (Fig. 4, F and G) and SEPT7-bound to SEPT7-free ratios (Fig. 4 H). The ratio of SEPT7-bound to SEPT7-free compartments (2.4 to 1) was the same for LBPA-negative and LBPA-positive GFP-CD63, and it was ∼50% lower than EEA1-positive GFP-CD63 (Fig. 4, D and H).

In spite of the strong preference of EEA1-positive GFP-CD63 compartments for septin-coated microtubules, septin-bound GFP-CD63 compartments were predominately positive for LBPA (71%) rather than EEA1 (31%) (Fig. 4 I). These percentages of LBPA-positive and EEA1-positive GFP-CD63 were nearly identical to those of the total GFP-CD63 population (Fig. 4 J). No difference was observed between the percentage of septin-bound CD63-GFP compartments that were EEA1-positive and LBPA-negative, or EEA1-negative and LBPA-positive (Fig. 4, K and L). In live MDCK cells, use of the pH-sensitive probe LysoView633, which labels compartments with pH ≤ 5.0, showed that 64% of septin-bound GFP-CD63 contained LysoView633 (Fig. S4, A and B). This percentage was similar to the percentage of all GFP-CD63 compartments that were LysoView633 positive (65%; Fig. S4 C). Moreover, it was consistent with 71% of septin-bound GFP-CD63 containing LBPA, which is present in acidified endolysosomes (Gruenberg, 2020; Kobayashi et al., 2002).

Next, we examined whether septin-coated microtubules harbor CD63-containing MVBs that contain RILP, a dynein adaptor that marks compartments that move retrogradely (Cantalupo et al., 2001), and Rab27a, which is recruited downstream of Rab7 priming MVBs for fusion with the plasma membrane (Verweij et al., 2022). The latter are mature MVBs that lack early and recycling endosome markers (EEA1, Rab5, and Rab11) (Verweij et al., 2022). First, we assessed the overall distribution of GFP-RILP with respect to SEPT7-coated microtubules. The preponderance of GFP-RILP–labeled compartments (80%) localized to SEPT7-coated microtubules, which indicated a strong preference for these tracks by endolysosomes that are retrogradely transported or anchored by the dynein–dynactin motor (Fig. 5, A–C). Although GFP-RILP endosomes were overall more LBPA positive than EEA1 positive, SEPT7-bound GFP-RILP had similar percentages of EEA1-positive and LBPA-positive endosomes (Fig. 5, D and E). Notably, EEA1-positive GFP-RILP

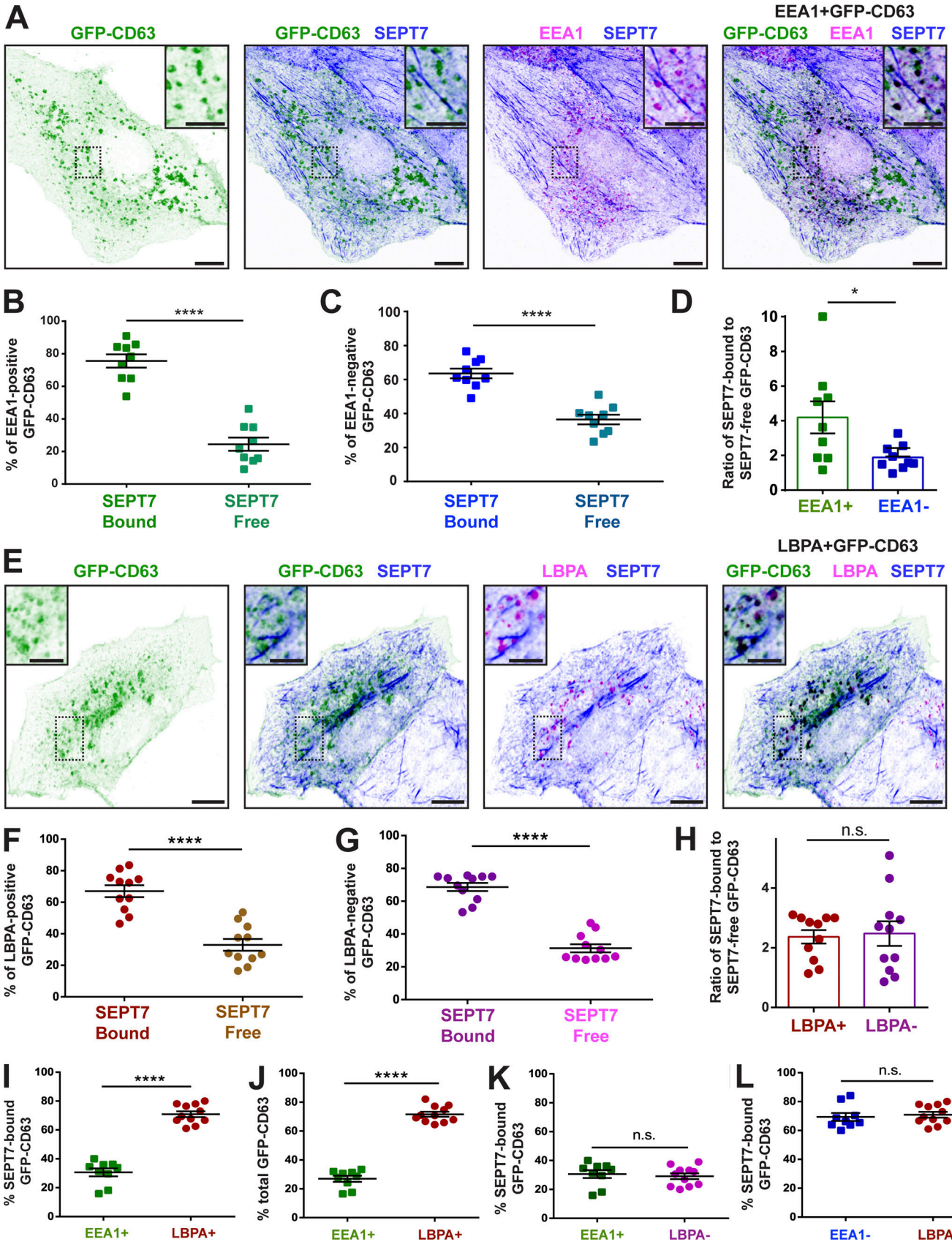

Figure 4. **A subset of EEA1-positive GFP-CD63 endosomes associate preferentially with septin-coated microtubules. (A)** Confocal microscopy images show single optical sections from subconfluent MDCK cells transfected with GFP-CD63 (inverted forest green), which were stained for endogenous SEPT7 (inverted blue) and EEA1 (inverted magenta). Overlap between GFP-CD63 and EEA1 is shown in black color. Insets show outlined regions (dashed rectangle) in

higher magnification. Scale bars, 10 and 5 µm (insets). **(B and C)** Quantification of the mean percentage (±SEM, error bars) of EEA1-positive (B) and EEA1-negative (C) GFP-CD63 endosomes that exhibit overlap (SEPT7-bound) or do not overlap with SEPT7 (SEPT7-free) filaments. Analysis was performed in MDCK cells transfected with GFP-CD63 and data (n = 9 cells) were analyzed with an unpaired t test with Welch's correction. **** P < 0.0001. **(D)** Mean ratios (±SEM, errors) of SEPT7-bound to SEPT7-free GFP-CD63 endosomes that were EEA1 positive or EEA1 negative in MDCK cells transfected with GFP-CD63. Data (n = 9 cells) were statistically analyzed with an unpaired t test with Welch's correction. * P < 0.05. **(E)** Confocal microscopy images show single optical sections from subconfluent MDCK cells transfected with GFP-CD63 (inverted forest green), which were stained for endogenous SEPT7 (inverted blue) and LBPA (inverted magenta). Overlap between GFP-CD63 and LBPA is shown in black color. Insets show outlined regions (dashed rectangle) in higher magnification. Scale bars, 10 and 5 µm (insets). **(F and G)** Quantification of the mean percentage (±SEM, error bars) of LBPA-positive (F) and LBPA-negative (G) GFP-CD63 endosomes that exhibit overlap (SEPT7-bound) or do not overlap with SEPT7 (SEPT7-free) filaments. Analysis was performed in MDCK-GFP-CD63 cells (n = 11) and data were analyzed with an unpaired t test with Welch's correction. **** P < 0.0001. **(H)** Mean ratios (±SEM, error bars) of SEPT7-bound to SEPT7-free GFP-CD63 endosomes that were LBPA positive or LBPA negative in MDCK cells transfected with GFP-CD63. Data (n = 9 cells) were statistically analyzed with a Mann-Whitney test. n.s., not significant. **(I and J)** Mean percentage (±SEM, error bars) of SEPT7-bound (I) and total (J) GFP-CD63 endosomes that were positive for EEA1 or LBPA. Analysis was performed in MDCK cells transfected with GFP-CD63 stained for endogenous EEA1 (n = 9 cells) or LBPA (n = 11 cells), and data were statistically analyzed with an unpaired t test with Welch's correction. **** P < 0.0001. **(K)** Mean percentage (±SEM, error bars) of SEPT7-bound GFP-CD63 endosomes that were positive for EEA1 or negative for LBPA. Analysis was performed in MDCK cells transfected with GFP-CD63 stained for endogenous EEA1 (n = 9 cells) or LBPA (n = 11 cells), and data were statistically analyzed with an unpaired t test with Welch's correction. n.s., not significant. **(L)** Mean percentage (±SEM, error bars) of SEPT7-bound GFP-CD63 endosomes that were negative for EEA1 or positive for LBPA. Analysis was performed in MDCK cells transfected with GFP-CD63 cells, and stained for endogenous EEA1 (n = 9 cells) or LBPA (n = 11 cells). Data were statistically analyzed with an unpaired t test with Welch's correction. n.s., not significant.

exhibited significantly higher ratios of SEPT7-bound to SEPT7-free compartments (11.5 to 1) compared with EEA1-negative GFP-RILP (3.3 to 1) (Fig. 5 F). In contrast, there was no difference in the ratios of SEPT7-bound to SEPT7-free compartments between LBPA-positive and LBPA-negative GFP-RILP (Fig. 5 G).

Unlike GFP-RILP, which extensively localized on septin-associated microtubules, mRuby3-Rab27a did not exhibit a preference for septin-coated microtubules. Quantification of the overall distribution of mRuby3-Rab27a showed a 50/50 split between SEPT7-bound and SEPT7-free compartments (Fig. 5, H–J). The SEPT7-bound GFP-CD63 compartments were also equally divided between mRuby3-Rab27a positive and negative, which mirrored the percentage of Rab27a-positive GFP-CD63 independent of septin association (Fig. 5, I and J). Additionally, the ratio of SEPT7-bound to SEPT7-free compartments did not vary between mRuby3-Rab27a positive and negative GFP-CD63 (Fig. 5 K). Taken together, these results show that a subset of EEA1-positive GFP-CD63 endosomes has a strong preference for septin-coated microtubules upstream of acquiring Rab27a, while the septin-bound GFP-CD63 endosomes are predominately acidified LBPA-positive endosomes. Thus, preferential association of EEA1-positive CD63 endosomes with septin-coated microtubules may aid in their transition to LBPA-positive MVBs/LEs, which populate septin-coated microtubules due to their restricted motility.

SEPT7 depletion enhances the motility of GFP-CD63 endosomes and impairs maturation into LBPA-positive MVBs/LEs

Biogenesis of MVBs/LEs occurs concomitantly with the retrograde traffic of early endosomes, which shift from peripheral to perinuclear areas of the cytoplasm as they transition to more acidic LEs and lysosomes (Bonifacino and Neefjes, 2017; Huotari and Helenius, 2011; Johnson et al., 2016; Winckler et al., 2018). Given the preferential association of EEA1-positive GFP-CD63 with septin-coated microtubules and the suppressed motility of GFP-CD63 on this microtubule subset, we tested how septin knockdown impacts the traffic and maturation of GFP-CD63 endosomes.

We used super-resolution spinning disk confocal microscopy to image and analyze the movement of GFP-CD63 in MDCK cells, which were transfected with control non-targeting and SEPT7-targeting shRNAs. SEPT7 shRNA reduced SEPT7 levels and abolished SEPT7 filaments, which was indicative of loss of microtubule-bound septins (Fig. S5, A and B). Staining for α-tubulin, however, showed no reduction in overlap of GFP-CD63 with microtubules, which indicates that SEPT7 does not impact association of GFP-CD63 endosomes with microtubules (Fig. S5, C and D). We analyzed GFP-CD63 motility in intracellular midzones, which were bordered by the inner and outward perimeters of 5-µm-wide zones from the plasma and nuclear membrane edges, respectively. We analyzed traffic in these regions, because first, these are primarily the cytoplasmic areas that endosomes traverse on microtubules, second, the high membrane density of the perinuclear cytosplasm may restrict motility independently of the microtubule cytoskeleton, and third, motility of endosomes in the peripheral cytoplasm is influenced by a network of actin stress fibers, which is in close proximity to the plasma membrane (Traikov et al., 2014). In SEPT7-depleted cells, movement of GFP-CD63 endosomes with velocities of <0.3 µm/s was visibly reduced (Fig. 6 A). Conversely, GFP-CD63 movements with velocities >0.5 µm/s were more abundant in SEPT7-depleted than control cells (Fig. 6 A and Videos 7 and 8). Consistent with a visually more motile GFP-CD63 (Fig. 6 A), the distribution of velocities shifted in SEPT7-depleted cells and the mean velocity of GFP-CD63 increased (Fig. 6 B). Similarly, the distribution of displacements showed a reduction in the 0–1 µm range, while the number 1–2.5 µm displacements increased (Fig. 6 C). Thus, microtubule-associated septins restricted the motility of GFP-CD63 between the perinuclear and peripheral regions of the cytoplasm, which was consistent with the arrest of GFP-CD63 motility on septin-coated microtubules in cell-free reconstitution assays (Fig. 3).

We next asked whether the enhanced motility of GFP-CD63 impacts the progressive maturation of early endosomes to MVBs/LEs by analyzing the percentage of GFP-CD63 endosomes with EEA1 and LBPA as respective markers of early/intermediary and late MVBs. SEPT7 knockdown did not alter the

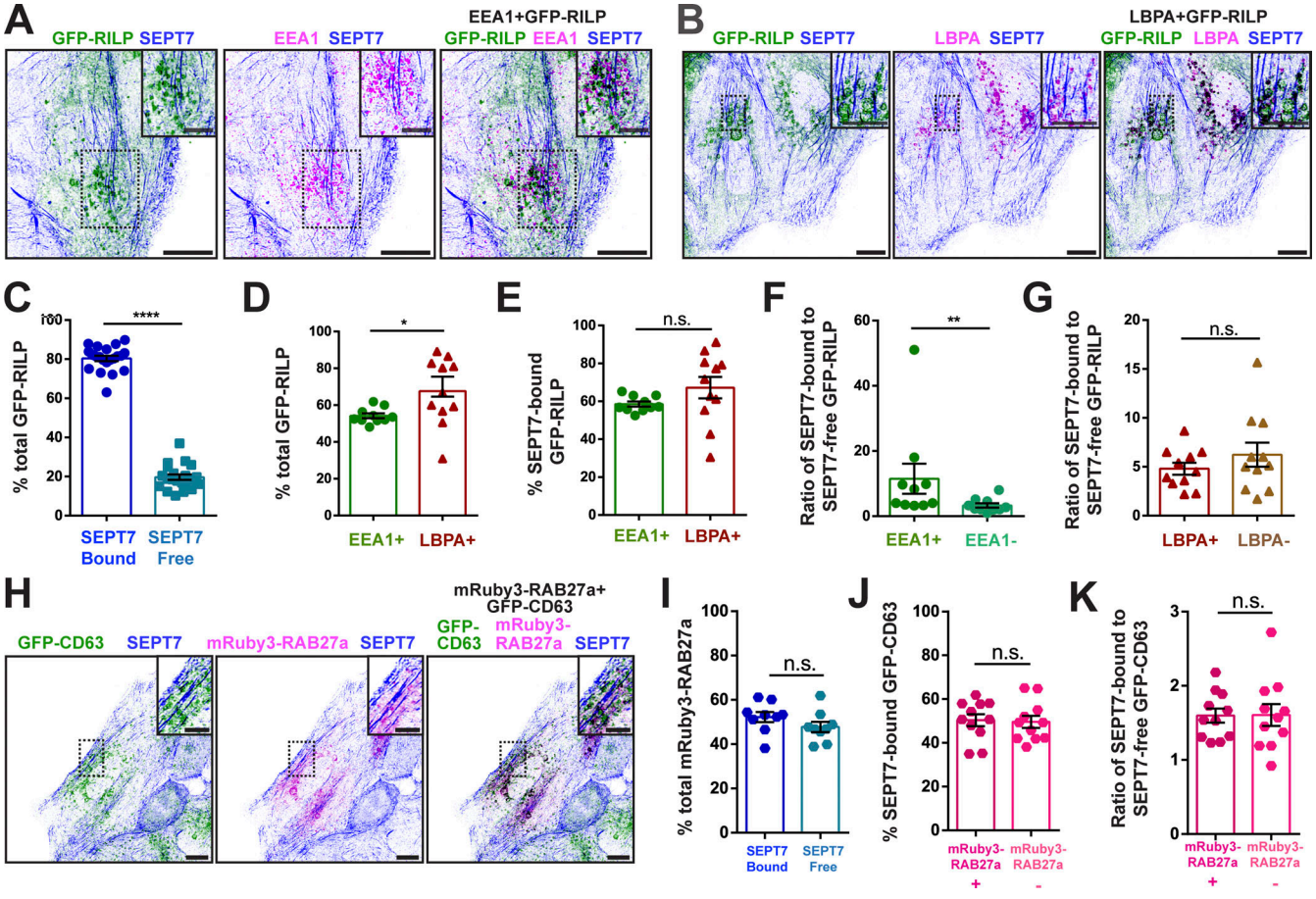

Figure 5. **EEA1- and RILP-positive endosomes are more extensively bound to septin-coated microtubules than LBPA- and Rab27a-containing MVBs.** **(A and B)** Maximum intensity projections of confocal microscopy z-series sections of subconfluent MDCK cells, which were transfected with GFP-RILP (inverted forest green) and stained for endogenous SEPT7 (inverted blue) and EEA1 (A; inverted magenta) or LPBA (B; inverted magenta). Scale bars, 10 and 5 µm (insets). **(C)** Mean percentage (±SEM, error bars) of GFP-RILP endosomes that overlap (SEPT7-bound) and do not overlap with SEPT7 (SEPT7-free). Quantification was performed in subconfluent MDCK cells (n = 21) which were transfected with GFP-RILP and stained for endogenous SEPT7. Data were analyzed with a Mann-Whitney test. **** $P < 0.0001$. **(D and E)** Mean percentage (±SEM, error bars) of total (D) and SEPT7-bound (E) GFP-RILP endosomes that contain EEA1 (EEA1+) and LBPA (LBPA+). Quantification was performed in subconfluent MDCK cells, which were transfected with GFP-RILP and stained for endogenous SEPT7, EEA1 (n = 10 cells), and LBPA (n = 11 cells). Data were analyzed with an unpaired t test with Welch's correction. n.s., not significant, * $P < 0.05$. **(F)** Mean ratios (±SEM, error bars) of SEPT7-bound to SEPT7-free GFP-RILP endosomes with or without EEA1. Quantification was performed in subconfluent MDCK cells (n = 10), which were transfected with GFP-RILP and stained for endogenous SEPT7 and EEA1. Data were analyzed with a Mann-Whitney test. ** $P < 0.01$. **(G)** Mean ratios (±SEM, error bars) of SEPT7-bound to SEPT7-free GFP-RILP endosomes with or without LBPA. Quantification was performed in subconfluent MDCK cells (n = 11), which were transfected with GFP-RILP and stained for endogenous SEPT7 and LBPA. Data were analyzed with a Mann-Whitney test. n.s., not significant. **(H)** Maximum intensity projections of confocal microscopy z-series sections of subconfluent MDCK-GFP-CD63 cells (inverted forest green), which were transfected with mRuby3-Rab27a (inverted magenta) and stained for endogenous SEPT7 (inverted blue). Scale bars, 10 and 5 µm (insets). **(I)** Mean percentage (±SEM, error bars) of total mRuby3-Rab27a endosomes with or without overlap with SEPT7 filaments (n = 11 cells). Data were analyzed with a Mann-Whitney test. n.s., not significant. **(J)** Mean percentage (±SEM, error bars) of SEPT7-bound GFP-CD63 with or without overlap with mRuby3-Rab27a endosomes (n = 11 cells). Data were analyzed with a Mann-Whitney test. n.s., not significant. **(K)** Mean ratios (±SEM, error bars) of SEPT7-bound to SEPT7-free GFP-CD63 endosomes with or without mRuby3-Rab27a. Quantification was performed in subconfluent MDCK-GFP-CD63 cells, which were transfected with mRuby3-Rab27a (n = 11 cells). Data were analyzed with an unpaired t test with Welch's correction. n.s., not significant.

percentage of EEA1-positive GFP-CD63 (20%), which was the same in both control and SEPT7-depleted cells (Fig. 6, D and F). In contrast, SEPT7 knockdown diminished the percentage of LBPA-positive GFP-CD63 from 78 to 54% (Fig. 6, E and G). Thus, SEPT7 depletion does not impact the population of EEA1-positive GFP-CD63 endosomes but impairs their transition to mature LBPA-positive MVBs/LEs. In agreement, SEPT7 depletion also reduced the percentage of acidic GFP-CD63 compartments. Using the chimeric reporter pHluorin_M153R-CD63-mScarlet, which labels red all CD63-containing membranes but fluoresces green only in a non-acidic environment (Sung et al., 2020), we found that SEPT7 depletion reduced the percentage of acidic GFP-negative compartments (Fig. S6, A and B). A decrease in acidic GFP-CD63 endosomes was also observed in a DQ Red BSA uptake assay, in which dequenching of DQ Red BSA occurs in LEs with lower pH (Fig. S6, C and D). To further test whether slowing down of GFP-CD63 motility is critical for maturation, we treated MDCK cells with the dynein inhibitor, dynarrestin, using a concentration (10 µM) and duration (30 min) that does not acutely arrest endosome motility (Hoing et al., 2018). This

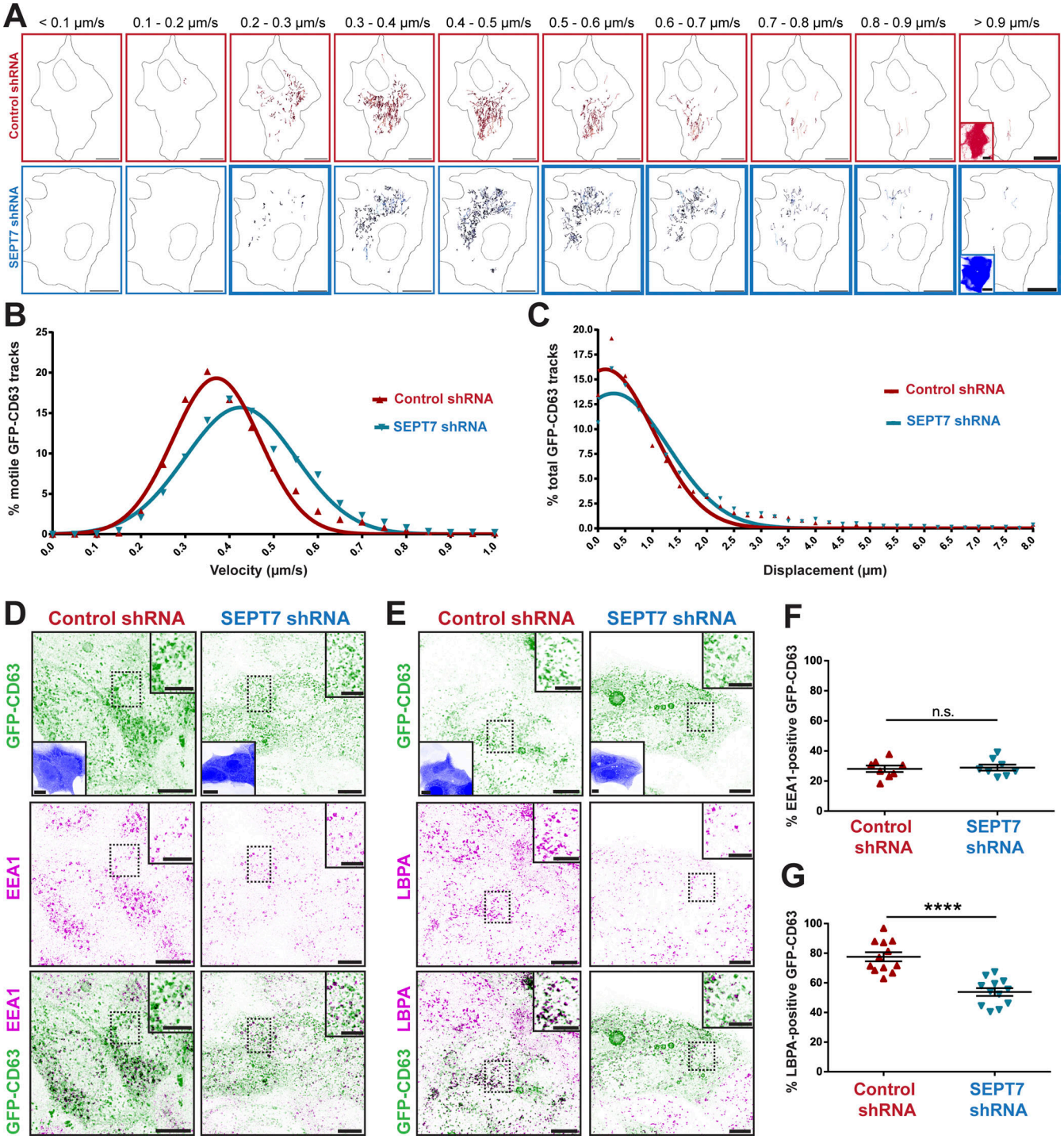

Figure 6. **Septins restrict the intracellular motility of GFP-CD63 endosomes and promote their maturation from EEA1- to LBPA-positive MVBs/LEs.** **(A)** Images show representative trajectories of motile GFP-CD63 endosomes with the indicated velocity ranges in the midzones of subconfluent MDCK cells, which were transfected with plasmids expressing mCherry (lower left insets) and control or SEPT7 shRNAs. Images show the cumulative trajectories of a 5-min acquisition by time-lapse super-resolution spinning disk confocal microscopy. Frames with thicker lines highlight the reduction in the abundance of trajectories with low velocities (0.2–0.3 µm/s) and an increase in the abundance of trajectories with higher velocities (>0.5 µm/s) in cells transfected with SEPT7 shRNAs. Scale bars, 10 µm. See also Videos 7 and 8. **(B)** Distribution of the velocity of GFP-CD63 in MDCK cells transfected with control (n = 2,640 endosomes from six cells) and SEPT7 shRNAs (n = 2,312 endosomes from six cells) fitted to a Gaussian non-linear regression line of best fit. **(C)** Distribution of displacements of GFP-CD63 in MDCK cells transfected with control (n = 2,640 endosomes from six cells) and SEPT7 shRNAs (n = 2,312 endosomes from six cells) fitted to a Gaussian non-linear regression line of best fit. **(D and E)** Maximum intensity projections of super-resolution confocal microscopy sections of subconfluent MDCK-GFP-CD63 cells (inverted forest green), which were stained for endogenous EEA1 (D; inverted magenta) or LBPA (E; inverted magenta) after transfection with plasmids that express mCherry (inverted blue) and control or SEPT7 shRNAs. Outlined regions (dashed rectangles) are shown in higher magnification (upper right insets). Lower left insets show the fluorescence of mCherry, which is coexpressed with shRNAs. Scale bars, 10 and 5 µm (insets). **(F)** Mean percentage

(±SEM, error bars) of total GFP-CD63 endosomes that overlap with EEA1 in MDCK-GFP-CD63 cells (n = 8) transfected with control or SEPT7 shRNAs. Data were statistically analyzed with an unpaired t test with Welch's correction. n.s., not significant. **(G)** Mean percentage (±SEM, error bars) of total GFP-CD63 endosomes that overlap with LBPA in MDCK-GFP-CD63 cells (n = 8) transfected with control or SEPT7 shRNAs. Data were statistically analyzed with an unpaired t test with Welch's correction. **** P < 0.0001.

treatment enhanced the percentage of LBPA-positive GFP-CD63 (Fig. S6, E and F). Taken together, these results suggest that immobilization of early/intermediary MVBs is a critical step of their biogenesis.

Discussion

Growing evidence indicates that organelles are positioned on microtubule tracks of distinct posttranslational modification, which modulate organelle motility and facilitate organelle–organelle contacts (Barlan and Gelfand, 2017; Mohan et al., 2019; Zheng et al., 2022). In addition to posttranslational modifications, MAPs also demarcate subsets of microtubules and regulate the movement of motors and their cargo (Atherton et al., 2013; Balabanian et al., 2018; Bodakuntla et al., 2019). However, the spatial distribution and function of MAPs in organelle positioning and dynamics are little studied and understood.

Septins are a family of multimerizing GTP-binding proteins, which associate with subsets of microtubules in a variety of cell types, but the functional significance of this interaction for the position and traffic of membrane organelles has not been explored (Spiliotis and Kesisova, 2021; Spiliotis and Nakos, 2021). Here, we analyzed the distribution of endosomal organelles with respect to a subset of microtubules, which are enriched with septins in MDCK epithelia. Using the ESCRT-I subunit TSG101, the lipid LBPA, and the tetraspanin CD63 as three independent MVB resident markers, we found that MVBs localize preferentially to septin-coated microtubules. Septin-bound GFP-CD63–carrying endosomes were predominately LBPA-positive indicating that septin-coated microtubules harbor mainly mature CD63-positive MVBs/LEs. Strikingly, however, EEA1-positive MVBs (GFP-CD63) have the highest ratio of septin-bound to septin-free compartments, which is nearly twofold higher than EEA1-negative or LBPA-positive CD63-containing MVBs/LEs, the overall population of which does not exhibit a preference for septin-coated over septin-free microtubules. These data suggest that early EEA1-positive MVBs have the highest preference for septin-associated microtubules and/or that a fraction of mature LBPA-positive MVBs dissociates from septin-bound microtubules upon merging with lysosomes, which have a lower fraction of septin-bound compartments.

In agreement with the preferential association of mature MVBs/LEs with septin-associated microtubules, we found that 80% of GFP-RILP is septin bound. Although a higher percentage of septin-bound RILP endosomes are LBPA positive rather than EEA1 positive, EEA1-positive GFP-RILP had a much higher ratio of SEPT7-bound to SEPT7-free than EEA1-negative GFP-RILP. Thus, similar to the EEA1-positive GFP-CD63 endosomes, EEA1-positive GFP-RILP compartments exhibit the highest localization to septin-associated microtubules. Given that RILP demarcates endosomes that have undergone a Rab5-to-Rab7 transition, EEA1-positive GFP-CD63 endosomes are likely MVBs in early stages of maturation or nascent LEs with low levels of LBPA. This interpretation is consistent with recent work, which reported that EEA1 is present in nearly half of Rab5-negative endosomes with ILVs and in LEs with phosphatidylinositol 3-phosphate (van der Beek et al., 2022). In contrast to the preference of EEA1-positive CD63 and RILP for septin-coated microtubules, Rab27a-positive compartments were equally distributed between septin-coated and septin-free microtubules. Therefore, MVBs destined for exocytosis do not have a preference for septin-associated microtubules, but half of the septin-bound MVBs are primed for exocytosis. These MVBs might be cued for exocytosis at perinuclear domains of the ventral or dorsal plasma membrane.

Septin depletion decreases the percentage of LBPA-positive GFP-CD63, a phenotype that is characterized by enhanced GFP-CD63 motility in intracellular regions between the peripheral and perinuclear cytoplasm. Taken together with the arrest of GFP-CD63 motility on microtubules decorated with recombinant septin complexes in cell-free assays, we posit that MVB maturation requires restriction of MVB motility by microtubule-associated septins. Interestingly, previous work in HeLa cells showed that the motility of AP-3–coated endosomes is restricted by peripheral actin-associated septins, which appeared to facilitate the recruitment of AP-3 and ESCRT-I/III to early endosomes (Traikov et al., 2014). In this study, SEPT7 knockdown reduced the degradation of the EGF receptor and there were fewer ILV-containing endosomes (Traikov et al., 2014). Recent work in *C. elegans* epidermis showed that MVB maturation involves anchoring to actin filaments by filamin (Shi et al., 2022), suggesting that immobilization of MVBs to the underlying cytoskeleton might be an evolutionarily conserved requirement for MVB maturation.

Endosomal maturation is linked to retrograde dynein-driven movement, but our data indicate that maturing CD63-containing endosomes immobilize on a subset of microtubules that is critical for progression to late endolysosomes. How does a model of endosomal maturation via retrograde flux reconcile with the immobilization of CD63-containing endosomes on septin-coated microtubules? First, retrograde flux does not preclude en route pausing and immobilization, which can be transient and overcome by switching into a motor that is not arrested by microtubule-associated septins. In this regard, early endosomes and MVBs can move retrogradely by the minus-end-directed KIFC1, which provides an alternative mechanism of transport to dynein–dynactin (Saito et al., 1997; Villari et al., 2020). Given that septin complexes have differential effects on kinesin and dynein motors (Suber et al., 2023), it is plausible that MVBs driven by either microtubule minus-end- or plus-end-directed kinesins are more motile on septin-coated microtubules at different stages of maturation. Second, immobilization might be

overcome through the recruitment of additional motors and their assembly into teams, which can jumpstart movement by exerting higher forces on endosomal cargos (Feng et al., 2018; Ferro et al., 2019; Klumpp and Lipowsky, 2005). Third, the EEA1-positive CD63- and RILP-containing compartments might be specialized endosomes, which are more closely related to LEs, and therefore, their immobilization occurs downstream of the centripetal movement of early endosomes.

We postulate that endosome immobilization on septin-coated microtubule tracks may facilitate organelle–organelle contacts between maturing MVBs and endolysosomes and the ER, which is involved in endosome biogenesis (Neefjes et al., 2017; Striepen and Voeltz, 2023). Thus, septin-coated microtubules may function similarly to detyrosinated microtubules, which restrict lysosome motility facilitating fusion with autophagosomes (Mohan et al., 2019). Beyond the exchange of cargo, which may include proteins involved in luminal acidification, organelle enlargement may also promote the recruitment and function of ESCRT proteins by reducing membrane tension, as recently reported (Mercier et al., 2020). Alternatively, immobilization may reduce endosomal membrane tension by relieving the forces exerted on the membrane of moving cargo by microtubule motors.

Microtubule-associated septins appear to be potent inhibitors of the motility of CD63-containing endosomes, raising the question of whether these endosomes are selectively targeted by septins. In MDCK epithelia, septin-coated microtubules underlie sites of vesicle exit from the Golgi complex and promote vesicle targeting to the developing apical and basal–lateral membranes (Spiliotis et al., 2008). In the proximal dendrites of hippocampal neurons, microtubule-associated septin 9 (SEPT9) restricts the mobility of KIF5C-driven vesicles with axonal cargo, while it promotes the anterograde transport of KIF1A-driven vesicles with dendritic cargo (Karasmanis et al., 2018). In vitro motility assays also show that microtubule-associated SEPT2/6/7 and SEPT2/6/7/9 complexes are more potent inhibitors of the dynein-dynactin-bicaudal D2 motor complex than KIF1A (Suber et al., 2023). These findings suggest that microtubule-associated septins can selectively suppress, permit, or enhance the movement of membrane organelles and vesicles depending on motor content.

In contrast to the immobilization of MVBs by microtubule-associated septins, we recently found that membrane-bound septin 9 promotes the retrograde movement of lysosomes by scaffolding dynein–dynactin motors (Kesisova et al., 2021). In addition, SEPT9 interacts with the ESCRT-I protein TSG101, which is critical for the functional assembly of ESCRT-III complexes on the intercellular bridge of dividing cells during cytokinetic abscission (Karasmanis et al., 2019). It is possible that septins function on the membrane of maturing endosomes and MVBs independently or in parallel with restricting motor motility on microtubule tracks. Septins may shift between microtubule tracks and endosomal membranes in response to signaling kinases, thereby switching functionally between microtubule-tethering factors and membrane cargo-motor adaptors (Spiliotis and Kesisova, 2021). However, these roles might not be mutually exclusive. Microtubule-binding proteins such as MAP6 and syntaphilin can associate with both microtubules and membrane cargo (Canty et al., 2023; Chen and Sheng, 2013; Tortosa et al., 2017). Moreover, association of cargo adaptors with MAPs such as the lysosomal adaptor TMEM106B with MAP6 or the dynein adaptor Spindle-F with the microtubule plus-end-binding protein Javelin-like provide mechanisms of cargo immobilization (Baskar et al., 2019; Otani et al., 2015; Schwenk et al., 2014). As septin multimers associate with one another in an end-to-end or side-to-side fashion, it is plausible that microtubule-associated septins interact with the septins of membrane organelles, forming a Velcro-like adhesion that immobilizes the latter in place. In this scenario, endosomes that carry membrane-bound septins are likely to move on septin-free microtubule tracks and arrest on septin-coated microtubules. Future work will explore the crosstalk between microtubule- and membrane-associated septins and the underlying mechanism that regulates their localization and functions.

In sum, our work shows that microtubules with a distinct molecular signature (septin-coated microtubules) promote the biogenesis of endosomal organelles by regulating their intracellular motility and position. Our findings add to recent evidence showing that organelle positioning and organelle–organelle contacts are regulated by microtubule tracks of distinct posttranslational modifications. Thus, the microtubule network provides instructive cues for organelle biogenesis and dynamics rather than passively scaffolding the distribution and movement of subcellular organelles.

Materials and methods

Cell culture, transfections, and treatments

MDCK II cells (RRID:CVCL_0424), renal (distal tubule) cells from normal female cocker spaniel and MDCK cell lines that stably express mCherry-SEPT9_i1 (Dolat et al., 2014) and GFP-CD63 were maintained in low glucose DMEM (Cat# D5523; Sigma-Aldrich) with 1 g/L $NaHCO_3$ (Cat# S5761; Sigma-Aldrich) and 10% FBS (Cat# S11150; R&D Systems), and 1% penicillin (P3032; Sigma-Aldrich), streptomycin (Cat# 11860-038; Gibco), and kanamycin (Cat# K4000; Sigma-Aldrich) at 37°C in a 5% CO_2 incubator. Cells were seeded at a density of 50,000–150,000 cells on 35-mm glass coverslips of #1.5 thickness (Cat# 48366-227; VWR) or 35-mm glass-bottom dishes (Cat# P35G-1.5-20-C; MatTek Life Sciences), which were precoated with 40 µg/ml type I bovine collagen PureCol (Cat# 5005; Advanced Biomatrix) in 0.1% glacial acetic acid (Cat# A6283; Sigma-Aldrich) for 5 min, then dried and rinsed twice with medium before cell plating. Cells were incubated with 10 µM dynarrestin (Cat# HY-121802; MedChemExpress) or DMSO (Cat# D2650; 1:500; Sigma-Aldrich) for 30 min. Dynarrestin was reconstituted with DMSO at a stock concentration of 5 mM and it was diluted in cell culture media.

Unless otherwise noted, cells were transfected with 0.5 µg of DNA using Lipofectamine 2000 (Cat# 11668019; Invitrogen) for 24 h before fixation or live-cell imaging, with a medium exchange occurring 4 h after transfection. For SEPT7 depletion experiments, cells were transfected with 0.5 µg of SEPT7 shRNA or scramble shRNA control using Lipofectamine 2000 (Cat# 11668019; Invitrogen) for 48 h, along with 0.5 µg of any

cotransfected DNA, with a medium exchange occurring 4 h after transfection. For live-cell imaging, cells were washed 3× with imaging media (FluoroBrite DMEM, Cat# A1896701; Gibco) supplemented with 10% FBS prior to being moved to the microscope environmental control chamber (maintained at 37°C in 5% CO_2).

For images in Fig. S5 A, mCherry-SEPT9_i1 MDCKs were transfected with 0.5 µg of CD63-GFP for 24 h, then treated with imaging media containing 1× concentration of LysoView 633 (Cat# 70058-T; Biotium), which was prepared in a 1,000× stock according to the manufacturer's instructions. Cells were protected from light and incubated at 37°C in 5% CO_2 for 20–30 min prior to time-lapse imaging.

A stable MDCK cell line expressing GFP-CD63 was generated as previously described (Bowen et al., 2011; Dolat et al., 2014; Karasmanis et al., 2019). Briefly, low passage MDCK II cells (RRID:CVCL_0424) were transfected with 0.5 µg of GFP-CD63 using Lipofectamine 2000 (Cat# 11668019; Invitrogen), then passaged continuously in low glucose DMEM with 1 g/L $NaHCO_3$ and 10% FBS, and 1% penicillin, streptomycin, and kanamycin at 37°C in a 5% CO_2 incubator. The medium was supplemented with 1 mg/ml geneticin (G418; Cat# A1720; Sigma-Aldrich) to select for G418 resistance. After 2 wk of selection, the cells were plated to 96-well plates and then separated based on expression level before clones were selected.

Visualization of acidified GFP-CD63 compartments was done by incubating MDCK-GFP-CD63 cells with 10 µg/ml of DQ Red BSA (Cat#D12051; Invitrogen) in FluoroBrite DMEM with 1% FBS Gibco for 6 h following 36–48 h of transfection with shRNA-expressing plasmid pSUPER_H1-TetO2.EBFP2 (see below). In separate experiments, shRNA plasmid (0.8 µg per 22 × 22 mm coverslip) was cotransfected with 0.2 µg pLenti-pHluorin_M153R-CD63-mScarlett (RRID: Addgene_172118).

Immunofluorescence

MDCKs were immunostained with the following antibodies: mouse anti-α-tubulin (DM1α, 1:500; T6199; RRID#AB_477583; Sigma-Aldrich), rat monoclonal anti-α-tubulin, tyrosinated, clone YL1/2 (1:100, MAB1864; RRID:AB_2210391; Sigma-Aldrich), rabbit polyclonal anti-detyrosinated α-tubulin (1:100, AB3201; RRID:AB_177350; Sigma-Aldrich), mouse anti-acetylated tubulin (1:500, T7451; RRID:AB_609894; Sigma-Aldrich), rabbit anti-SEPT7 (1:300; 18991; RRID:AB_10705434; IBL America), mouse anti-TSG101 (4A10, 1:100; GTX635396; RRID:AB_2888524; GeneTex), mouse anti-EEA1 (1:100; 610456; RRID:AB_397829; BD Biosciences), mouse anti-LBPA (1:100; Z-PLBPA; RRID:AB_11129226; Echelon Biosciences), rabbit anti-LAMTOR4/C7orf59 (1:200; Cat# 12284; RRID:AB_2797870; Cell Signaling). In Fig. S2 B, staining of MDCK cells with rabbit antibodies against detyrosinated α-tubulin (RRID:AB_177350) and SEPT7 (RRID:AB_10705434) was performed after conjugating the primary anti-SEPT7 to Alexa Fluor 594 using the Zenon Alex Fluor 594 rabbit IgG labeling kit (Cat# Z25307, RRID:AB_477583; Thermo Fisher Scientific). The F(ab')2 fragment affinity-purified secondary antibodies (1:200) included donkey anti-mouse and -rabbit antibodies conjugated with Alexa 488 (Cat# 715-546-150 and 711-546-152; RRID:AB_2340849 and RRID:AB_2340619; Jackson ImmunoResearch), Alexa594 (Cat# 715-586-151 and 711-586-152; RRID:AB_2340866 and RRID:AB_2340622; Jackson ImmunoResearch) or Alexa647 (Cat# 715-606-150 and 711-606-152; RRID:AB_2340866 and RRID:AB_2340625; Jackson ImmunoResearch). In Fig. S3, actin filaments were labeled by adding Phalloidin-iFluor 647 (Cat# ab176759; Abcam) to the incubation mix with the secondary antibodies.

Cells were fixed with warm 2% PFA (Cat# 15710; Electron Microscopy Sciences) in PBS (Cat# P4417; Sigma-Aldrich) for 12 min and quenched in 1× PBS with 0.25% ammonium chloride for 10 min. Cells were simultaneously blocked with 2% BSA (Cat# A9647; Sigma-Aldrich) and permeabilized with 0.3% saponin (Cat# 558255; EMD Millipore) wt/vol in 1× PBS at room temperature for 30 min. Primary antibodies were spun at 50,000 × *g* for 10 min at 4°C before incubation overnight at 4°C, while secondary antibodies were spun in the same manner prior to incubation at room temperature for 1 h. All antibodies were diluted in 1× PBS containing 2% BSA (Cat# A9647; Sigma-Aldrich) and 0.3% saponin (Cat# 558255; EMD Millipore) to maintain permeabilization during staining. Cells were then washed with 1× PBS before being mounted in FluorSave hard mounting medium (Cat# 345789; EMD Millipore) and allowed to dry for 1.5 h prior to imaging or storage at 4°C overnight.

In Fig. 1, A and F; Fig. S2; Fig. S3, A–E; and Fig. S5 C, cells were fixed with warm 2% PFA in PHEM buffer (60 mM PIPES, 25 mM HEPES, 10 mM EGTA, 2 mM MgCl2, pH 6.9) for 12 min, then quenched, blocked, permeabilized, stained, and mounted as described above.

In Fig. 1 C, costains for rabbit anti-SEPT7 (RRID:AB_10705434) and rabbit anti-LAMTOR4 (RRID:AB_2797870) were performed using the Zenon Alexa Fluor 594 rabbit IgG labeling kit (Cat# Z25307, RRID:AB_477583; Thermo Fisher Scientific) in accordance with the manufacturer's instructions. Cells were fixed, quenched, blocked, and permeabilized as described above, with rabbit anti-SEPT7 being incubated with the cells overnight at 4°C. Anti-rabbit Alexa Fluor 488 (Cat#711-546-152, RRID:AB_2340619; Jackson ImmunoResearch) was applied as a secondary, as described above, the following day. Afterward, 1 µg of rabbit anti-LAMTOR4 antibody was incubated with 5 µl of the Zenon rabbit IgG labeling kit (Cat# Z25351; Thermo Fisher Scientific) and then with 5 µl of Zenon rabbit blocking reagent in PBS for 5 min at room temperature. After dilution in the blocking buffer of 2% BSA (Cat# A9647; Sigma-Aldrich) and 0.3% saponin (Cat# 558255; EMD Millipore), the resulting complexes were incubated with cells for 1 h at room temperature. Cells were washed with PBS, mounted in FluorSave hard mounting medium (Cat# 345789; EMD Millipore), and imaged immediately.

Plasmids and cloning

The plasmid EGFP-RILP was purchased from Addgene (RRID:Addgene_110498) and was a gift from Terence Dermody and Bernardo Mainou (Vanderbilt University, Nashville, TN, USA; Mainou and Dermody, 2012). The plasmid pBS L30 mRuby3-Rab27A was purchased from Addgene (RRID:Addgene_166432) and was a gift from Raphael Gaudin (Montpellier University, Montpellier, France). The plasmid GFP-EEA1 wt was purchased

from Addgene (RRID:Addgene_42307) and was a gift from Silivia Corvera (UMass Chen Medical School, Worcester, MA, USA; Lawe et al., 2000). The plasmid CD63-pEGFP C2 was purchased from Addgene (RRID:Addgene_62964) and was a gift from Paul Luzio (Cambridge University, Cambridge, UK). The plasmid pEGFP-α-tubulin was a kind gift from James Nelson (Stanford University, Stanford, CA, USA; Barth et al., 2002). The plasmid pLenti-pHluorin_M153R-CD63-mScarlet was purchased from Addgene (RRID: Addgene_172118) and was a gift from Alissa Weaver (Vanderbilt School of Medicine, Nashville, TN, USA; Sung et al., 2020). The plasmids (RRID:Addgene_174497 and RRID:Addgene_174498) used for the expression and purification of the mCherry-tagged SEPT2/6/7 and SEPT2/6/7/9 complexes were as recently described (Iv et al., 2021; Nakos et al., 2019; Suber et al., 2023) and were gifts from Manos Mavrakis (Institut Fresnel, Marseille, France). The plasmid for the expression of mCherry-MAP4(654–1090) was made previously (Karasmanis et al., 2018).

For SEPT7 depletion experiments, an shRNA was generated targeting the predicted canine sequence of SEPT7 mRNA. Primers were ordered from IDT (forward: 5′-GATCCCCACAACAGAACTCTTCCAGATTCAAGAGATCTGGAAGAGTTCTGTTGTTTTTTA-3′, reverse: 5′-GGGCTTGTTGTCTTGAGAAGGTAAGTTCTCTACCTTCTCAAGACAACAAGAAAAATTCGA-3′). A scramble control based on a scrambled version of the shRNA sequence was also generated (forward: 5′-GATCCCCACCAACTTAACGCACAGATTTCAAGAGAATCTGTGCGTTAAGTTGGTTTTTTA-3′, reverse: 5′-GGGTGGTTGAATTGCGAGTCTAAAGTTCTCTTAGACACGCAATTCAACCAAAAAATTCGA-3′). These oligos were annealed and inserted into pSUPER-mCherry (Dolat et al., 2014) using the BglII and HindIII cut sites. Plasmid sequences were confirmed through sequencing (Genewiz).

The pSUPER plasmid that coexpressed EBFP2 and scramble control or SEPT7 shRNA was made by replacing the GFP sequence of a modified version of the plasmid pSUPER.gfp+neo (Cat#VEC-pBS-0006; Oligoengine), which included two sets of the Tet operon inserted between the EcoRI and HindIII sites at the end of the H1 promoter (pSUPER_H1-TetO2.gfp), with the sequence of EBFP2. The latter was amplified from the plasmid EBFP2 (RRID:Addgene_54665; a gift from Michael Davidson, Florida State University, Tallahassee, FL, USA) using Gibson cloning with forward primer 5′-CAGCCCAAGCTAGCTTACCGGTCGCCACCATGGTGAGCAAGGGCGAGGAGCTGTTC-3′ and reverse primer 5′-TCCGGACTTGTACAGCGGCCGCTACTTGTACAGCTCGTCCATGCCGAGAGTG-3′. After digestion of pSUPER.gfp+neo with HindIII, the amplified products were ligated with Gibson cloning. The new vector (pSUPER_H1-TetO2.EBFP2) was digested with BglII and HindIII for inserting primers with control and SEPT7-targetting shRNA sequences. The following primers were used: 5′-GATCCCCACCAACTTAACGCACAGATTTCAAGAGAATCTGTGCGTTAAGTTGGTTTTTTA-3′ (control shRNA forward), 5′-AGCTTAAAAAACCAACTTAACGCACAGATTCTCTTGAAATCTGAGCGTTAAGTTGGTGGG-3′, 5′-GATCCCCGAACAACAGAACTCTTCCATTCAAGAGATGGAAGAGTTCTGTTGTTCTTTTTA-3′ (control shRNA reverse), 5′-GATCCCCGAACAACAGAACTCTTCCATTCAAGAGATGGAAGAGTTCTGTTGTTCTTTTTA-3′ (SEPT7 shRNA forward), and 5′-AGCTTAAAAAGAACAACAGAACTCTTCCATCTCTTGAATGGAAGAGTTCTGTTGTTCGGG-3′ (SEPT7 shRNA reverse).

Isolation of GFP-CD63 endosomes from MDCK cells

MDCK-GFP-CD63 stable cells were cultured on four 15-cm dishes to 80–90% confluency, then washed twice with room temperature PBS 1× prior to removal with a cell scrapper in 5 ml of PBS 1×. Cells were spun at 200 × *g* for 5 min to pellet prior to resuspension in 2 ml of ice-cold motility assay buffer (10 mM PIPES, 50 mM KoAc, 4 mM MgCl2, 1 mM EGTA, 8.5% sucrose, pH 7.0) supplemented with 10 mM DTT, 1 mM PMSF, 1:50 of 10× mammalian protease inhibitor cocktail (VWR), and 1 mM ATP (Cat#BSA04-001; Cytoskeleton Inc). Cells were then passed through a custom Balch-style ball-bearing homogenizer 20 times while on ice. Afterward, the lysate was collected and spun successively at 4°C in the following sequence: 1,000 × *g* for 20 min (nuclear pellet), 4,356 × *g* for 30 min (mitochondrial and large membrane pellet), and 25,000 × *g* for 60 min (endosomal pellet). Each pellet was resuspended in 50 µl of the ice-cold motility assay buffer used during homogenization. Pellets were equilibrated overnight on ice before being gently resuspended with a cut pipette tip. A portion of the resuspended fractions (10 µl) was imaged to confirm that the endosomal fraction possessed the strongest GFP-CD63 signal and assess the quality of homogenization. The endosomal fraction was kept on ice and used within 48 h of isolation.

In vitro motility assays

Stabilized microtubules were generated by combining 80% unlabeled porcine brain tubulin (Cat# T238P; Cytoskeleton Inc), 10% porcine brain tubulin conjugated with HiLyte647 (Cat# TL670M; Cytoskeleton Inc), AMCA (Cat# TL440M; Cytoskeleton Inc) or biotin (Cat# T333P; Cytoskeleton Inc) in BRB80 (80 mM PIPES, 2 mM $MgCl_2$, 1 mM EGTA, 10% glycerol, pH 6.9 in double distilled [dd] H_2O) supplemented with 1 mM of GTP (Cat# BST06; Cytoskeleton Inc) and incubated at 37°C for 30 min. Subsequently, 10 µM of taxol (Cat# TXD01; Cytoskeleton Inc) was added to the mix, which was then incubated for another 15 min at 37°C. The final concentrated mix was stored at room temperature and protected from light, with working stocks being made at a 1:100 dilution.

Motility chambers were created by adhering acid-washed #1.5 35-mm glass coverslips to slides using double stick tape placed to create a channel ∼10 µl in volume. To adhere the taxol-stabilized microtubules to the coverslip, 2× the chamber volume of 5 mg/ml biotinylated BSA in cold ddH_2O was flowed into each chamber and incubated for 5 min followed by a wash of BRB80 at 10× the chamber volume. Subsequently, 2× the chamber volume of 0.5 mg/ml NeutrAvidin Biotin-binding Protein (Cat# A2666; Thermo Fisher Scientific) in cold PBS was flowed into each chamber and incubated for 5 min, similarly followed by a wash with BRB80. The diluted taxol-stabilized microtubule mix (2× the chamber volume) was then added and incubated for 10 min before a washout of BRB80. At this point, a running buffer was generated by mixing 0.5% wt/vol Pluronic F-127 (Cat #P2443; Sigma-Aldrich), 0.1 mg/ml BSA, 0.2 mg/ml casein (Cat #C7078; Sigma-Aldrich) and 10 µM taxol in the motility assay

buffer. Motility chambers were blocked with motility assay buffer containing 1 mg/ml BSA and 1% wt/vol Pluronic F-127, which was flowed into the chamber at 10× the chamber volume and incubated for a minimum of 10 min.

The isolated GFP-CD63–positive endosomes were diluted 1:10 into a motility mix (motility assay buffer supplemented with 2 mM ATP and 10% of an oxygen scavenging system consisting of 3.5 mg/ml Catalase, 4.5 mg/ml D-Glucose, 20 mg/ml Glucose Oxidase, and 30 mM β-mercaptoethanol). When conditions called for microtubules coated with recombinant septin complexes (prepared as described in Suber et al. [2023]), adhered and blocked microtubules were incubated with mCherry-SEPT2/6/7 or mCherry-SEPT2/6/7/9 diluted in motility assay buffer to specified concentrations for 10 min mCherry-MAP4-MTBD (654–1090) (prepared as described in Karasmanis et al. [2018]) was applied in the same fashion. After a washout of BRB80 followed by running buffer, the motility mix was flowed into the chamber and sealed with vacuum grease at the openings. The motility of GFP-CD63 positive endosomes was recorded using time-lapse TIRF microscopy performed at room temperature at 2 fps for 1 min.

Microscopy

Cells in Fig. 1, B–E; and Fig. 4, A and E, were imaged on an Olympus FluoView 1000 inverted confocal laser-scanning microscope equipped with three Hamamatsu R7862 photomultiplier tubes and multiline argon ion (458, 488, and 515 nm), helium-neon (543 nm), and diode 401- and 635-nm lasers. Images were acquired using an Olympus PlanApo 60×/1.42-NA oil objective, 0.2 µm step size for z-stack collection, and FV10-ASW 02.01 software.

Cells in Fig. 1, A and F; Fig. 5, A, B, and H; Fig. 6, D and E; Fig. S1 B; Fig. S2; Fig. S3; Fig. S4 A; Fig. S5 C; and Fig. S6, A and E, were imaged on a Leica Stellaris 5 inverted DMi8 confocal laser-scanning microscope equipped with 4 Power HyD-S detectors, six solid-state laser lines (405, 448, 488, 514, 561, and 638 nm), a tandem FOV and 8 kHz resonance scanner, and motorized stage. Images were acquired using an HC PL APO 63×/1.4 NA oil CS2 immersion objective, zoom of 1×-3×, and 0.3-µm step size for z-stack collection. Images were processed with the LIGHTNING deconvolution module within the LAS X STELLARIS software for enhanced lateral resolution. Live-cell images in Fig. S4 A were captured inside a stage-top Okolab environmental control chamber with a Tokai Hit STX stage-top incubator (37°C, 5% CO_2).

Time-lapse videos used for analysis in Fig. 2, F and G, were imaged on an inverted Olympus IX83 spinning disk confocal system equipped with a Yokogawa CSU 10 spinning disk, a motorized stage, solid-state 405-, 488-, 561-, and 635-nm laser lines, a Hamamatsu Orca Flash 4 CMOS camera, and an Okolab environmental control chamber (37°C, 5% CO_2). Images were acquired using an Olympus 60×/1.49-NA oil objective and the VisiView software.

Cells in Fig. S5 A were imaged on a Zeiss AxioObserver Z1 inverted wide-field microscope equipped with a Zeiss 63×/1.4-NA oil objective, a Hamamatsu Orca-R2 CCD camera, and the Slidebook 6.0 software.

All TIRF microscopy (in vitro motility assays, Fig. 3, A–D; and Videos 4, 5, and 6) was performed with the TIRF module of a Deltavision OMX V4 inverted microscope using an Olympus PlanApo 60×/1.49 NA oil immersion objective, six solid-state laser lines (405, 445, 488, 514, 568, 642 nm), and three cCMOS pco.edge cameras (PCO) along with the OMX Master Acquisition and the softWoRx 6.1 reconstruction software.

Time lapse videos in Fig. 2, A–D, were captured on an inverted Nikon Ti2E confocal microscope equipped with a Yokogawa CSU-W1 SoRa spinning disk, motorized stage, multilaser system with 405-, 488-, 568-, and 647-nm lines, an Okolab environmental control chamber (37°C, 5% CO_2), and a Hamamatsu Orca Fusion CMOS camera. Images were acquired using a Nikon Apo TIRF 60×/1.49-NA oil objective. For movies in Fig. 6, A–D, the camera was swapped for a Hamamatsu Orca QUEST qCMOS camera and the objective was replaced with a Nikon Apo TIRF 100×/1.49-NA oil objective. Images were processed with the denoising module within the NIS-Elements software used for image capture.

Fig. S1 A images were taken on an Olympus Elyra 7 super-resolution system equipped on an inverted AxioObserver 7 microscope with a motorized stage, Elyra 7 laser module equipped with 405-, 488-, 561-, and 642-nm lines, an Incubator XL dark S1 environmental control chamber (37°C, 5% CO_2), and a pco.edge 4.2 sCMOS camera. Images were acquired using a Plan-Apochromat 63×/1.40 NA oil objective and processed within the ZEN imaging software.

In Fig. 6 C, images of living cells were taken with a Nikon TiE2 inverted microscope equipped with a Yokogawa CSU-W1 spinning disk, motorized stage, multilaser system with 405-, 488-, 568-, and 647-nm lines, an Okolab Oko UNO environmental control chamber, which was set at 37°C and 5% CO_2, and a Hamamatsu ORCA-Fusion BT CMOS camera. Images were acquired using a Nikon CFI APO 100×/60×/1.49-NA oil objective.

Image processing, analyses, and quantifications

All image processing and analysis were conducted using the FIJI/ImageJ 1.53s (RRID:SCR_002285) open-source analysis software. Any added plugins or macros beyond the standard installation package are noted below. All inverted Look Up Tables (LUTs) used for images were downloaded from the NeuroCyto LUT package developed by Christophe Leterrier (Neuropathophysiology Institute, Marseille, France; https://www.github.com/cleterrier/ChrisLUTs).

In Fig. 1, A and F; Fig. S1, A and B; and Fig. S3, D and E, the overlap pseudochannel images were generated with the AND function of the Image Calculator command to keep only the overlapping pixels in each parent channel.

Quantifying endosomal compartments along septin filaments with traditional colocalization analysis proves challenging since filament-associated endosomes often display a lumen (which results in no fluorescent pixels to overlap with the filament fluorescence), are often imaged to the side of filaments (resulting in minimal overlap but positive association), and markers are often bound to additional non-endosomal membranes in the cell like the plasma membrane (resulting in false positives). To quantify the number of endosomes associated with septin filaments in fixed cells (Figs. 1, 4, and 5), targeted endosomal

markers were manually outlined along their limiting membrane. The outlines were combined into a region of interest (ROI) that was overlaid with the septin channel and manually scored for positive association with filaments generating a new ROI set using the click-to-delete macro written by Kees Straatman (University of Leicester; https://www.github.com/KeesStraatman/Delete-ROI) in 2014. This analysis was limited to septin filaments and excluded septin puncta or clusters that overlapped with endosomal membrane proteins. If the quantified image contained a z-stack, only the slice that represented the preponderancy of in-plane endosomes and septin filaments was analyzed to avoid the false overlays of endosomes and filaments in different planes that would otherwise occur in a maximum intensity projection.

If a second endosomal marker was present (Figs. 4 and 5), the outlines were also scored for the presence or absence of the second marker prior to scoring filament association, generating additional ROI sets. AND/OR functions were used to combine ROI outlines to determine all subpopulations of targeted endosomal markers. In Fig. 6, the cells were outlined according to the mCherry fill and GFP-CD63 within the outline was scored for the presence of EEA1 and LBPA as described above. In Fig. S4, a single image was taken of the live cell environment and quantified as above. In Fig. S5 D, GFP-CD63 was scored along immunostained tubulin filaments, rather than septin filaments.

To analyze the movement of endosomes in relation to septin filaments (Fig. 2, F and G), three equal-sized ROIs for each cell were generated in areas of rich mCherry-SEPT9_i1 filaments. Each ROI was then analyzed using the TrackMate Plugin (LoG detector, estimated object diameter of 0.4 µm, simple Linear Assignment Problem tracker, 0.5-µm linking distance, 0.5-µm gap closing distance, and a filter for track quality >5) to generate an overlay of the vesicle behavior over the course of 60 s (20 frames). These tracks were then overlaid onto the filament channel of the first frame tracked and scored as immotile/motile (motile defined as a final displacement greater than its own diameter) and bound/unbound to the filament.

To define motile vesicular behavior along septin filaments (Fig. 2 E), kymographs were generated along the first frame of mCherry-SEPT9_i1 filaments and were visually analyzed for the percentage of tracks that fell into unidirectional (continuous motility in a single direction), bidirectional (multiple directional changes with robust run lengths in each direction), and diffusive (rapid directional changes with minimal overall displacement) categories over the course of the 3-min (720 frames) movie.

In Fig. 6, TrackMate was used to analyze GFP-CD63 movement in SEPT7 scramble control or shRNA-depleted cells. To avoid analyzing endosomes close to the plasma membrane (and thus potentially moving under actin-based motility instead of microtubule motors), an ROI was generated 5 µm from the plasma membrane by scaling down the cell outline. Likewise, an ROI excluding the crowded (and relatively non-motile) perinuclear zone was also generated by scaling up the nuclear outline 5 µm past the nuclear envelope. The remaining area of the cell (5 µm from the plasma membrane and excluding the surrounding 5 µm area of the nucleus) was designated as the mid-zone ROI for TrackMate analysis with the following parameters: LoG detector, estimated object diameter of 0.75 µm to account for enlarged vesicles in the shRNA depletion conditions, simple LAP tracker, 0.8 µm linking distance, 0.8 µm gap closing distance. In addition, filters were set for a number of gaps (<4), minimum track duration (10 s), and mean track quality (0.7 or greater). The resulting track characteristics were categorized into bins based on velocity (total track distance/time) or total displacement and analyzed statistically.

In vitro assay analysis (Fig. 3) was conducted by generating kymographs along the length of each microtubule using a custom macro in FIJI/ImageJ that also subtracted background (rolling ball radius of 50 px), and applied a Gaussian blur filter (Sigma-Aldrich of 0.75) to each channel. Each kymograph was scored for a total number of GFP-CD63 tracks present, the movement characteristics of each track (immotile or motile), and stability when associated with the microtubules (number of disassociation events during tracking, number of landing events during tracking). Landing frequency was calculated as number of landing events on an individual microtubule divided by the length of the microtubule and the duration of the video (1 min). Disassociation, processive, and stationary frequencies were calculated in the same manner. Velocities of motile GFP-CD63 on the kymograph were calculated using the Velocity Measurement macro developed by Volker Baecker (INSERM, Montpellier RIO Imaging; https://dev.mri.cnrs.fr/projects/imagej-macros/wiki/Velocity_Measurement_Tool).

Statistical analysis

Statistical analysis of data and graph generation was performed with GraphPad Prism 6 (RRID:SCR_002798) statistical analysis software. The individual values of all data sets are displayed in all bar graphs including those of Fig. 3, which contain data points that cannot be distinguished from the x-axis owing to their low values. Data sets were assessed for normal distribution of variance using the D'Agostino and Pearson normality test and comparing for agreement with the Shapiro-Wilk normality test. For pair-wise comparisons of non-parametric normally distributed data, P values were calculated using an unpaired *t* test with Welch's correction, while non-parametric non-normally distributed data used a Mann-Whitney test. P values <0.05 were considered statistically significant. In Fig. 6, B and C, binned data was plotted on a points-only XY graph and a non-linear regression line was fitted to each condition using a Gaussian equation. To plot pair-wise data graphs, the scatterplot with bar column graphs was used to display the mean and ± standard error of mean (SEM). *N* and P values for each analysis are denoted in the corresponding figure legend.

Reproducibility and replicability

In Fig. 1, results were representative of immunofluorescence experiments with antibodies against endogenous SEPT7 and EEA1, LAMTOR4, TSG101, LBPA, and GFP-CD63, which were independently repeated in four (EEA1), three (LAMTOR4), ten (TSG101), seven (LBPA), and six (CD63) experiments. MDCK stains for endogenous SEPT7 and microtubules were repeated at least six different times. In Fig. 2, imaging experiments of GFP-CD63 motility with respect to mCherry-SEPT9_i1 were

representative of at least three independent experiments with different microscope platforms (spinning disk and laser scanning confocal), and GFP-EEA1 motility was captured by spinning disk microscopy in two independent experiments. In Fig. 3, data were analyzed from eight different time-lapse videos with 29–50 uncoated microtubules each, five different videos with 43–50 mCherry-SEPT2/6/7–coated microtubules each, seven different videos with 25–5 mCherry-SEPT2/6/7/9–coated microtubules each, and seven different videos with 29–60 mCherry-MAP4-MTBD–coated microtubules each. In Fig. 4, staining of MDCK-GFP-CD63 cells with antibodies against endogenous SEPT7, EEA1, and LBPA were independently repeated at least five times, two of which were with different secondary antibodies. In Fig. 5, A–G, two independent experiments were performed with staining for endogenous LBPA and SEPT7 in MDCK cells transfected with GFP-RILP. In Fig. 5, H–K, three independent experiments of mRuby3-Rab27a expression in MDCK-GFP-CD63 were performed, and SEPT7 was stained with two different secondaries in separate experiments. In Fig. 6, A–C, data were collected from nine to ten different image fields and time-lapse series per condition. In Fig. 6, D–F, results are representative from three experiments.

Online supplemental material

Fig. S1 shows mCherry-SEPT9_i1 localization to subsets of microtubules labeled with α-tubulin-GFP and anti-α-tubulin. Fig. S2 shows SEPT7 localization with respect to tyrosinated, detyrosinated, and acetylated microtubules. Fig. S3 shows the localization of SEPT7 with respect to actin filaments and GFP-CD63–containing endosomes. Fig. S4 shows the localization and quantification of GFP-CD63 endosomes that contain the acidic pH probe LysoView 633 with respect to septin filaments. Fig. S5 shows images and quantification of endogenous SEPT7, and the overlap between GFP-CD63 and microtubules in MDCK cells treated with control and SEPT7 shRNAs. Fig. S6 shows that SEPT7 depletion reduces the percentage of acidic GFP-CD63 endosomes, and that treatment of MDCK cells with the dynein inhibitor dynarrestin increases the percentage of LBPA-positive GFP-CD63. Video 1 shows examples of immotile GFP-CD63 endosomes on mCherry-SEPT9_i1 filaments. Video 2 shows examples of GFP-CD63 endosomes shifting between neighboring mCherry-SEPT9_i1 filaments. Video 3 shows the processive movement of GFP-CD63 along an mCherry-SEPT9_i1 filament. Video 4 shows the processive movement of a GFP-CD63 endosome along an uncoated microtubule in a cell-free in vitro reconstitution assay. Video 5 shows the pausing of motile GFP-CD63 at microtubule-associated mCherry-SEPT2/6/7 in a cell-free reconstitution assay. Video 6 shows the immobilization of GFP-CD63 on microtubules coated with mCherry-SEPT2/6/7/9 in a cell-free reconstitution assay. Video 7 shows GFP-CD63 dynamics in live MDCK cells treated with control shRNA. Video 8 shows GFP-CD63 movement in live MDCK cells treated with SEPT7 shRNA.

Data availability

All the data underlying this study are available in the published article and its online supplemental material.

Acknowledgments

We thank Dr. Yani Suber for help and advice with the in vitro motility assays, and Drs. Harini Sreenivasappa and Andrew Schaefer for help with microscopy. Microscopy was performed at Drexel University's Cell Imaging Center (RRID: SCR_022689). We thank Jesse DeWitt from Nikon Instruments, Inc. for the use of the SORA spinning disk microscopy. We also thank Alma Arnold, James Shaw, and Colleen Mote from Zeiss for the use of the Zeiss Elyra 7 microscope with lattice SIM^2.

This work was supported by the National Institutes of Health/National Institute of General Medical Sciences grants 5R01GM097664 and 5R35G136337 to E.T. Spiliotis.

Author contributions: Conceptualization, E.T. Spiliotis and B.P. Robinson; Methodology: E.T. Spiliotis, B.P. Robinson, and P. Bhakt; Validation: B.P. Robinson, N.R. Bass, and E.T. Spiliotis; Formal Analysis, B.P. Robinson, N.R. Bass, and E.T. Spiliotis; Investigation, B.P. Robinson, N.R. Bass, and E.T. Spiliotis; Resources: B.P. Robinson and P. Bhakt; Data Curation, B.P. Robinson and E.T. Spiliotis; Writing—Original Draft: E.T. Spiliotis and B.P. Robinson, Writing—Review & Editing: E.T. Spiliotis and B.P. Robinson; Visualization: B.P. Robinson, N.R. Bass, and E.T. Spiliotis; Supervision, E.T. Spiliotis and B.P. Robinson; Project Administration: E.T. Spiliotis; and Funding acquisition: E.T. Spiliotis.

Disclosures: The authors declare no competing interests exist.

Submitted: 9 August 2023
Revised: 6 February 2024
Accepted: 10 April 2024

References

Alonso, A., and F.M. Goñi. 2018. The physical properties of ceramides in membranes. *Annu. Rev. Biophys.* 47:633–654. https://doi.org/10.1146/annurev-biophys-070317-033309

Andreu, Z., and M. Yáñez-Mó. 2014. Tetraspanins in extracellular vesicle formation and function. *Front. Immunol.* 5:442. https://doi.org/10.3389/fimmu.2014.00442

Atherton, J., A. Houdusse, and C. Moores. 2013. MAPping out distribution routes for kinesin couriers. *Biol. Cell.* 105:465–487. https://doi.org/10.1111/boc.201300012

Babst, M. 2011. MVB vesicle formation: ESCRT-dependent, ESCRT-independent and everything in between. *Curr. Opin. Cell Biol.* 23:452–457. https://doi.org/10.1016/j.ceb.2011.04.008

Bai, X., J.R. Bowen, T.K. Knox, K. Zhou, M. Pendziwiat, G. Kuhlenbäumer, C.V. Sindelar, and E.T. Spiliotis. 2013. Novel septin 9 repeat motifs altered in neuralgic amyotrophy bind and bundle microtubules. *J. Cell Biol.* 203:895–905. https://doi.org/10.1083/jcb.201308068

Balabanian, L., A.R. Chaudhary, and A.G. Hendricks. 2018. Traffic control inside the cell: Microtubule-based regulation of cargo transport. *Biochemist.* 40:14–17. https://doi.org/10.1042/BIO04002014

Barlan, K., and V.I. Gelfand. 2017. Microtubule-based transport and the distribution, tethering, and organization of organelles. *Cold Spring Harb. Perspect. Biol.* 9:a025817. https://doi.org/10.1101/cshperspect.a025817

Barth, A.I., K.A. Siemers, and W.J. Nelson. 2002. Dissecting interactions between EB1, microtubules and APC in cortical clusters at the plasma membrane. *J. Cell Sci.* 115:1583–1590. https://doi.org/10.1242/jcs.115.8.1583

Baskar, R., A. Bahkrat, T. Otani, H. Wada, G. Davidov, H. Pandey, L. Gheber, R. Zarivach, S. Hayashi, and U. Abdu. 2019. The plus-tip tracking and microtubule stabilizing activities of Javelin-like regulate microtubule organization and cell polarity. *FEBS J.* 286:3811–3830. https://doi.org/10.1111/febs.14944

Baust, T., M. Anitei, C. Czupalla, I. Parshyna, L. Bourel, C. Thiele, E. Krause, and B. Hoflack. 2008. Protein networks supporting AP-3 function in targeting lysosomal membrane proteins. *Mol. Biol. Cell*. 19:1942–1951. https://doi.org/10.1091/mbc.e08-02-0110

Benoit, B., C. Poüs, and A. Baillet. 2023. Septins as membrane influencers: Direct play or in association with other cytoskeleton partners. *Front. Cell Dev. Biol.* 11:1112319. https://doi.org/10.3389/fcell.2023.1112319

Bobrie, A., M. Colombo, G. Raposo, and C. Théry. 2011. Exosome secretion: Molecular mechanisms and roles in immune responses. *Traffic*. 12: 1659–1668. https://doi.org/10.1111/j.1600-0854.2011.01225.x

Bodakuntla, S., A.S. Jijumon, C. Villablanca, C. Gonzalez-Billault, and C. Janke. 2019. Microtubule-associated proteins: Structuring the cytoskeleton. *Trends Cell Biol.* 29:804–819. https://doi.org/10.1016/j.tcb.2019.07.004

Bonifacino, J.S., and J. Neefjes. 2017. Moving and positioning the endolysosomal system. *Curr. Opin. Cell Biol.* 47:1–8. https://doi.org/10.1016/j.ceb.2017.01.008

Bowen, J.R., D. Hwang, X. Bai, D. Roy, and E.T. Spiliotis. 2011. Septin GTPases spatially guide microtubule organization and plus end dynamics in polarizing epithelia. *J. Cell Biol.* 194:187–197. https://doi.org/10.1083/jcb.201102076

Cannon, K.S., B.L. Woods, and A.S. Gladfelter. 2017. The unsolved problem of how cells sense micron-scale curvature. *Trends Biochem. Sci.* 42:961–976. https://doi.org/10.1016/j.tibs.2017.10.001

Cantalupo, G., P. Alifano, V. Roberti, C.B. Bruni, and C. Bucci. 2001. Rab-interacting lysosomal protein (RILP): The Rab7 effector required for transport to lysosomes. *EMBO J.* 20:683–693. https://doi.org/10.1093/emboj/20.4.683

Canty, J.T., A. Hensley, M. Aslan, A. Jack, and A. Yildiz. 2023. TRAK adaptors regulate the recruitment and activation of dynein and kinesin in mitochondrial transport. *Nat. Commun.* 14:1376. https://doi.org/10.1038/s41467-023-36945-8

Cavini, I.A., D.A. Leonardo, H.V.D. Rosa, D.K.S.V. Castro, H. D'Muniz Pereira, N.F. Valadares, A.P.U. Araujo, and R.C. Garratt. 2021. The structural biology of septins and their filaments: An update. *Front. Cell Dev. Biol.* 9: 765085. https://doi.org/10.3389/fcell.2021.765085

Chadwick, S.R., S. Grinstein, and S.A. Freeman. 2021. From the inside out: Ion fluxes at the centre of endocytic traffic. *Curr. Opin. Cell Biol.* 71:77–86. https://doi.org/10.1016/j.ceb.2021.02.006

Chen, Y., and Z.H. Sheng. 2013. Kinesin-1-syntaphilin coupling mediates activity-dependent regulation of axonal mitochondrial transport. *J. Cell Biol.* 202:351–364. https://doi.org/10.1083/jcb.201302040

Clague, M.J., and S. Urbé. 2008. Multivesicular bodies. *Curr. Biol.* 18: R402–R404. https://doi.org/10.1016/j.cub.2008.02.068

Clague, M.J., S. Urbé, F. Aniento, and J. Gruenberg. 1994. Vacuolar ATPase activity is required for endosomal carrier vesicle formation. *J. Biol. Chem.* 269:21–24. https://doi.org/10.1016/S0021-9258(17)42302-7

Collinet, C., M. Stöter, C.R. Bradshaw, N. Samusik, J.C. Rink, D. Kenski, B. Habermann, F. Buchholz, R. Henschel, M.S. Mueller, et al. 2010. Systems survey of endocytosis by multiparametric image analysis. *Nature*. 464:243–249. https://doi.org/10.1038/nature08779

Danson, C.M., N. Pearson, K.J. Heesom, and P.J. Cullen. 2018. Sorting nexin-21 is a scaffold for the endosomal recruitment of huntingtin. *J. Cell Sci.* 131: jcs211672. https://doi.org/10.1242/jcs.211672

Dolat, L., J.L. Hunyara, J.R. Bowen, E.P. Karasmanis, M. Elgawly, V.E. Galkin, and E.T. Spiliotis. 2014. Septins promote stress fiber-mediated maturation of focal adhesions and renal epithelial motility. *J. Cell Biol.* 207: 225–235. https://doi.org/10.1083/jcb.201405050

Dolat, L., and E.T. Spiliotis. 2016. Septins promote macropinosome maturation and traffic to the lysosome by facilitating membrane fusion. *J. Cell Biol.* 214:517–527. https://doi.org/10.1083/jcb.201603030

Doole, F.T., S. Gupta, T. Kumarage, R. Ashkar, and M.F. Brown. 2023. Biophysics of membrane stiffening by cholesterol and phosphatidylinositol 4,5-bisphosphate (PIP2). *Adv. Exp. Med. Biol.* 1422:61–85. https://doi.org/10.1007/978-3-031-21547-6_2

Fader, C.M., and M.I. Colombo. 2009. Autophagy and multivesicular bodies: Two closely related partners. *Cell Death Differ.* 16:70–78. https://doi.org/10.1038/cdd.2008.168

Falguières, T., P.P. Luyet, C. Bissig, C.C. Scott, M.C. Velluz, and J. Gruenberg. 2008. In vitro budding of intralumenal vesicles into late endosomes is regulated by Alix and Tsg101. *Mol. Biol. Cell*. 19:4942–4955. https://doi.org/10.1091/mbc.e08-03-0239

Feng, Q., K.J. Mickolajczyk, G.Y. Chen, and W.O. Hancock. 2018. Motor reattachment kinetics play a dominant role in multimotor-driven cargo transport. *Biophys. J.* 114:400–409. https://doi.org/10.1016/j.bpj.2017.11.016

Ferro, L.S., S. Can, M.A. Turner, M.M. ElShenawy, and A. Yildiz. 2019. Kinesin and dynein use distinct mechanisms to bypass obstacles. *Elife*. 8: e48629. https://doi.org/10.7554/eLife.48629

Froidevaux-Klipfel, L., F. Poirier, C. Boursier, R. Crépin, C. Poüs, B. Baudin, and A. Baillet. 2011. Modulation of septin and molecular motor recruitment in the microtubule environment of the Taxol-resistant human breast cancer cell line MDA-MB-231. *Proteomics*. 11:3877–3886. https://doi.org/10.1002/pmic.201000789

Froidevaux-Klipfel, L., B. Targa, I. Cantaloube, H. Ahmed-Zaïd, C. Poüs, and A. Baillet. 2015. Septin cooperation with tubulin polyglutamylation contributes to cancer cell adaptation to taxanes. *Oncotarget*. 6: 36063–36080. https://doi.org/10.18632/oncotarget.5373

Gruenberg, J. 2020. Life in the lumen: The multivesicular endosome. *Traffic*. 21:76–93. https://doi.org/10.1111/tra.12715

Guardia, C.M., G.G. Farías, R. Jia, J. Pu, and J.S. Bonifacino. 2016. BORC functions upstream of kinesins 1 and 3 to coordinate regional movement of lysosomes along different microtubule tracks. *Cell Rep.* 17: 1950–1961. https://doi.org/10.1016/j.celrep.2016.10.062

Hanson, P.I., and A. Cashikar. 2012. Multivesicular body morphogenesis. *Annu. Rev. Cell Dev. Biol.* 28:337–362. https://doi.org/10.1146/annurev-cellbio-092910-154152

Hendricks, A.G., E. Perlson, J.L. Ross, H.W. Schroeder III, M. Tokito, and E.L. Holzbaur. 2010. Motor coordination via a tug-of-war mechanism drives bidirectional vesicle transport. *Curr. Biol.* 20:697–702. https://doi.org/10.1016/j.cub.2010.02.058

Henne, W.M., N.J. Buchkovich, and S.D. Emr. 2011. The ESCRT pathway. *Dev. Cell*. 21:77–91. https://doi.org/10.1016/j.devcel.2011.05.015

Henne, W.M., H. Stenmark, and S.D. Emr. 2013. Molecular mechanisms of the membrane sculpting ESCRT pathway. *Cold Spring Harb. Perspect. Biol.* 5: a016766. https://doi.org/10.1101/cshperspect.a016766

Höing, S., T.Y. Yeh, M. Baumann, N.E. Martinez, P. Habenberger, L. Kremer, H.C.A. Drexler, P. Küchler, P. Reinhardt, A. Choidas, et al. 2018. Dynarrestin, a novel inhibitor of cytoplasmic dynein. *Cell Chem. Biol.* 25: 357–369.e6. https://doi.org/10.1016/j.chembiol.2017.12.014

Hu, J., X. Bai, J.R. Bowen, L. Dolat, F. Korobova, W. Yu, P.W. Baas, T. Svitkina, G. Gallo, and E.T. Spiliotis. 2012. Septin-driven coordination of actin and microtubule remodeling regulates the collateral branching of axons. *Curr. Biol.* 22:1109–1115. https://doi.org/10.1016/j.cub.2012.04.019

Huotari, J., and A. Helenius. 2011. Endosome maturation. *EMBO J.* 30: 3481–3500. https://doi.org/10.1038/emboj.2011.286

Iv, F., C.S. Martins, G. Castro-Linares, C. Taveneau, P. Barbier, P. Verdier-Pinard, L. Camoin, S. Audebert, F.C. Tsai, L. Ramond, et al. 2021. Insights into animal septins using recombinant human septin octamers with distinct SEPT9 isoforms. *J. Cell Sci.* 134:jcs258484. https://doi.org/10.1242/jcs.258484

Johnson, D.E., P. Ostrowski, V. Jaumouillé, and S. Grinstein. 2016. The position of lysosomes within the cell determines their luminal pH. *J. Cell Biol.* 212:677–692. https://doi.org/10.1083/jcb.201507112

Jongsma, M.L., J. Bakker, B. Cabukusta, N. Liv, D. van Elsland, J. Fermie, J.L. Akkermans, C. Kuijl, S.Y. van der Zanden, L. Janssen, et al. 2020. SKIP-HOPS recruits TBC1D15 for a Rab7-to-Arl8b identity switch to control late endosome transport. *EMBO J.* 39:e102301. https://doi.org/10.15252/embj.2019102301

Jongsma, M.L.M., N. Bakker, and J. Neefjes. 2023. Choreographing the motor-driven endosomal dance. *J. Cell Sci.* 136:jcs259689. https://doi.org/10.1242/jcs.259689

Karasmanis, E.P., D. Hwang, K. Nakos, J.R. Bowen, D. Angelis, and E.T. Spiliotis. 2019. A septin double ring controls the spatiotemporal organization of the ESCRT machinery in cytokinetic abscission. *Curr. Biol.* 29: 2174–2182.e7. https://doi.org/10.1016/j.cub.2019.05.050

Karasmanis, E.P., C.T. Phan, D. Angelis, I.A. Kesisova, C.C. Hoogenraad, R.J. McKenney, and E.T. Spiliotis. 2018. Polarity of neuronal membrane traffic requires sorting of kinesin motor cargo during entry into dendrites by a microtubule-associated septin. *Dev. Cell*. 46:204–218.e7. https://doi.org/10.1016/j.devcel.2018.06.013

Katzmann, D.J., G. Odorizzi, and S.D. Emr. 2002. Receptor downregulation and multivesicular-body sorting. *Nat. Rev. Mol. Cell Biol.* 3:893–905. https://doi.org/10.1038/nrm973

Keren-Kaplan, T., and J.S. Bonifacino. 2021. ARL8 relieves SKIP autoinhibition to enable coupling of lysosomes to kinesin-1. *Curr. Biol.* 31: 540–554.e5. https://doi.org/10.1016/j.cub.2020.10.071

Kesisova, I.A., B.P. Robinson, and E.T. Spiliotis. 2021. A septin GTPase scaffold of dynein-dynactin motors triggers retrograde lysosome transport. *J. Cell Biol.* 220:e202005219. https://doi.org/10.1083/jcb.202005219

Klumperman, J., and G. Raposo. 2014. The complex ultrastructure of the endolysosomal system. *Cold Spring Harb. Perspect. Biol.* 6:a016857. https://doi.org/10.1101/cshperspect.a016857

Klumpp, S., and R. Lipowsky. 2005. Cooperative cargo transport by several molecular motors. *Proc. Natl. Acad. Sci. USA.* 102:17284–17289. https://doi.org/10.1073/pnas.0507363102

Kobayashi, T., M.H. Beuchat, J. Chevallier, A. Makino, N. Mayran, J.M. Escola, C. Lebrand, P. Cosson, T. Kobayashi, and J. Gruenberg. 2002. Separation and characterization of late endosomal membrane domains. *J. Biol. Chem.* 277:32157–32164. https://doi.org/10.1074/jbc.M202838200

Krokowski, S., D. Lobato-Márquez, A. Chastanet, P.M. Pereira, D. Angelis, D. Galea, G. Larrouy-Maumus, R. Henriques, E.T. Spiliotis, R. Carballido-López, and S. Mostowy. 2018. Septins recognize and entrap dividing bacterial cells for delivery to lysosomes. *Cell Host Microbe.* 24: 866–874.e4. https://doi.org/10.1016/j.chom.2018.11.005

Kuzmić, M., G. Castro Linares, J. Leischner Fialová, F. Iv, D. Salaün, A. Llewellyn, M. Gomes, M. Belhabib, Y. Liu, K. Asano, et al. 2022. Septin-microtubule association via a motif unique to isoform 1 of septin 9 tunes stress fibers. *J. Cell Sci.* 135:jcs258850. https://doi.org/10.1242/jcs.258850

Lawe, D.C., V. Patki, R. Heller-Harrison, D. Lambright, and S. Corvera. 2000. The FYVE domain of early endosome antigen 1 is required for both phosphatidylinositol 3-phosphate and Rab5 binding. Critical role of this dual interaction for endosomal localization. *J. Biol. Chem.* 275: 3699–3705. https://doi.org/10.1074/jbc.275.5.3699

Magiera, M.M., and C. Janke. 2014. Post-translational modifications of tubulin. *Curr. Biol.* 24:R351–R354. https://doi.org/10.1016/j.cub.2014.03.032

Mainou, B.A., and T.S. Dermody. 2012. Transport to late endosomes is required for efficient reovirus infection. *J. Virol.* 86:8346–8358. https://doi.org/10.1128/JVI.00100-12

Matsuo, H., J. Chevallier, N. Mayran, I. Le Blanc, C. Ferguson, J. Fauré, N.S. Blanc, S. Matile, J. Dubochet, R. Sadoul, et al. 2004. Role of LBPA and Alix in multivesicular liposome formation and endosome organization. *Science.* 303:531–534. https://doi.org/10.1126/science.1092425

Mercier, V., J. Larios, G. Molinard, A. Goujon, S. Matile, J. Gruenberg, and A. Roux. 2020. Endosomal membrane tension regulates ESCRT-III-dependent intra-lumenal vesicle formation. *Nat. Cell Biol.* 22:947–959. https://doi.org/10.1038/s41556-020-0546-4

Mohan, N., E.M. Sorokina, I.V. Verdeny, A.S. Alvarez, and M. Lakadamyali. 2019. Detyrosinated microtubules spatially constrain lysosomes facilitating lysosome-autophagosome fusion. *J. Cell Biol.* 218:632–643. https://doi.org/10.1083/jcb.201807124

Mostowy, S., and P. Cossart. 2012. Septins: The fourth component of the cytoskeleton. *Nat. Rev. Mol. Cell Biol.* 13:183–194. https://doi.org/10.1038/nrm3284

Nakos, K., M.R. Radler, and E.T. Spiliotis. 2019. Septin 2/6/7 complexes tune microtubule plus-end growth and EB1 binding in a concentration- and filament-dependent manner. *Mol. Biol. Cell.* 30:2913–2928. https://doi.org/10.1091/mbc.E19-07-0362

Neefjes, J., M.M.L. Jongsma, and I. Berlin. 2017. Stop or go? Endosome positioning in the establishment of compartment architecture, dynamics, and function. *Trends Cell Biol.* 27:580–594. https://doi.org/10.1016/j.tcb.2017.03.002

O'Loughlin, T., T.A. Masters, and F. Buss. 2018. The MYO6 interactome reveals adaptor complexes coordinating early endosome and cytoskeletal dynamics. *EMBO Rep.* 19:e44884. https://doi.org/10.15252/embr.201744884

Otani, T., K. Oshima, A. Kimpara, M. Takeda, U. Abdu, and S. Hayashi. 2015. A transport and retention mechanism for the sustained distal localization of Spn-F-IKKε during Drosophila bristle elongation. *Development.* 142: 2338–2351. https://doi.org/10.1242/dev.130674

Park, J.H., and A. Roll-Mecak. 2018. The tubulin code in neuronal polarity. *Curr. Opin. Neurobiol.* 51:95–102. https://doi.org/10.1016/j.conb.2018.03.001

Piper, R.C., and D.J. Katzmann. 2007. Biogenesis and function of multivesicular bodies. *Annu. Rev. Cell Dev. Biol.* 23:519–547. https://doi.org/10.1146/annurev.cellbio.23.090506.123319

Pols, M.S., and J. Klumperman. 2009. Trafficking and function of the tetraspanin CD63. *Exp. Cell Res.* 315:1584–1592. https://doi.org/10.1016/j.yexcr.2008.09.020

Poteryaev, D., S. Datta, K. Ackema, M. Zerial, and A. Spang. 2010. Identification of the switch in early-to-late endosome transition. *Cell.* 141: 497–508. https://doi.org/10.1016/j.cell.2010.03.011

Raposo, G., and W. Stoorvogel. 2013. Extracellular vesicles: Exosomes, microvesicles, and friends. *J. Cell Biol.* 200:373–383. https://doi.org/10.1083/jcb.201211138

Rink, J., E. Ghigo, Y. Kalaidzidis, and M. Zerial. 2005. Rab conversion as a mechanism of progression from early to late endosomes. *Cell.* 122: 735–749. https://doi.org/10.1016/j.cell.2005.06.043

Saito, N., Y. Okada, Y. Noda, Y. Kinoshita, S. Kondo, and N. Hirokawa. 1997. KIFC2 is a novel neuron-specific C-terminal type kinesin superfamily motor for dendritic transport of multivesicular body-like organelles. *Neuron.* 18:425–438. https://doi.org/10.1016/S0896-6273(00)81243-X

Schwenk, B.M., C.M. Lang, S. Hogl, S. Tahirovic, D. Orozco, K. Rentzsch, S.F. Lichtenthaler, C.C. Hoogenraad, A. Capell, C. Haass, and D. Edbauer. 2014. The FTLD risk factor TMEM106B and MAP6 control dendritic trafficking of lysosomes. *EMBO J.* 33:450–467. https://doi.org/10.1002/embj.201385857

Shi, L., Y. Jian, M. Li, T. Hao, C. Yang, and X. Wang. 2022. Filamin FLN-2 promotes MVB biogenesis by mediating vesicle docking on the actin cytoskeleton. *J. Cell Biol.* 221:e202201020. https://doi.org/10.1083/jcb.202201020

Song, K., G. Russo, and M. Krauss. 2016. Septins as modulators of endolysosomal membrane traffic. *Front. Cell Dev. Biol.* 4:124. https://doi.org/10.3389/fcell.2016.00124

Spiliotis, E.T., S.J. Hunt, Q. Hu, M. Kinoshita, and W.J. Nelson. 2008. Epithelial polarity requires septin coupling of vesicle transport to polyglutamylated microtubules. *J. Cell Biol.* 180:295–303. https://doi.org/10.1083/jcb.200710039

Spiliotis, E.T., and I.A. Kesisova. 2021. Spatial regulation of microtubule-dependent transport by septin GTPases. *Trends Cell Biol.* 31:979–993. https://doi.org/10.1016/j.tcb.2021.06.004

Spiliotis, E.T., M. Kinoshita, and W.J. Nelson. 2005. A mitotic septin scaffold required for Mammalian chromosome congression and segregation. *Science.* 307:1781–1785. https://doi.org/10.1126/science.1106823

Spiliotis, E.T., and K. Nakos. 2021. Cellular functions of actin- and microtubule-associated septins. *Curr. Biol.* 31:R651–R666. https://doi.org/10.1016/j.cub.2021.03.064

Striepen, J.F., and G.K. Voeltz. 2023. Endosome biogenesis is controlled by ER and the cytoskeleton at tripartite junctions. *Curr. Opin. Cell Biol.* 80: 102155. https://doi.org/10.1016/j.ceb.2023.102155

Suber, Y., M.N.A. Alam, K. Nakos, P. Bhakt, and E.T. Spiliotis. 2023. Microtubule-associated septin complexes modulate kinesin and dynein motility with differential specificities. *J. Biol. Chem.* 299:105084. https://doi.org/10.1016/j.jbc.2023.105084

Sung, B.H., A. von Lersner, J. Guerrero, E.S. Krystofiak, D. Inman, R. Pelletier, A. Zijlstra, S.M. Ponik, and A.M. Weaver. 2020. A live cell reporter of exosome secretion and uptake reveals pathfinding behavior of migrating cells. *Nat. Commun.* 11:2092. https://doi.org/10.1038/s41467-020-15747-2

Targa, B., L. Klipfel, I. Cantaloube, J. Salameh, B. Benoit, C. Poüs, and A. Baillet. 2019. Septin filament coalignment with microtubules depends on SEPT9_i1 and tubulin polyglutamylation, and is an early feature of acquired cell resistance to paclitaxel. *Cell Death Dis.* 10:54. https://doi.org/10.1038/s41419-019-1318-6

Tortosa, E., Y. Adolfs, M. Fukata, R.J. Pasterkamp, L.C. Kapitein, and C.C. Hoogenraad. 2017. Dynamic palmitoylation targets MAP6 to the axon to promote microtubule stabilization during neuronal polarization. *Neuron.* 94:809–825.e7. https://doi.org/10.1016/j.neuron.2017.04.042

Traikov, S., C. Stange, T. Wassmer, P. Paul-Gilloteaux, J. Salamero, G. Raposo, and B. Hoflack. 2014. Septin6 and Septin7 GTP binding proteins regulate AP-3- and ESCRT-dependent multivesicular body biogenesis. *PLoS One.* 9:e109372. https://doi.org/10.1371/journal.pone.0109372

van der Beek, J., C. de Heus, N. Liv, and J. Klumperman. 2022. Quantitative correlative microscopy reveals the ultrastructural distribution of endogenous endosomal proteins. *J. Cell Biol.* 221:e202106044. https://doi.org/10.1083/jcb.202106044

van Niel, G., S. Charrin, S. Simoes, M. Romao, L. Rochin, P. Saftig, M.S. Marks, E. Rubinstein, and G. Raposo. 2011. The tetraspanin CD63 regulates ESCRT-independent and -dependent endosomal sorting during melanogenesis. *Dev. Cell.* 21:708–721. https://doi.org/10.1016/j.devcel.2011.08.019

Verweij, F.J., M.P. Bebelman, A.E. George, M. Couty, A. Bécot, R. Palmulli, X. Heiligenstein, J. Sirés-Campos, G. Raposo, D.M. Pegtel, and G. van Niel. 2022. ER membrane contact sites support endosomal small GTPase conversion for exosome secretion. *J. Cell Biol.* 221:e202112032. https://doi.org/10.1083/jcb.202112032

Villari, G., C. Enrico Bena, M. Del Giudice, N. Gioelli, C. Sandri, C. Camillo, A. Fiorio Pla, C. Bosia, and G. Serini. 2020. Distinct retrograde microtubule

motor sets drive early and late endosome transport. *EMBO J.* 39:e103661. https://doi.org/10.15252/embj.2019103661

von Zastrow, M., and A. Sorkin. 2021. Mechanisms for regulating and organizing receptor signaling by endocytosis. *Annu. Rev. Biochem.* 90:709–737. https://doi.org/10.1146/annurev-biochem-081820-092427

Winckler, B., V. Faundez, S. Maday, Q. Cai, C. Guimas Almeida, and H. Zhang. 2018. The endolysosomal system and proteostasis: From development to degeneration. *J. Neurosci.* 38:9364–9374. https://doi.org/10.1523/JNEUROSCI.1665-18.2018

Woods, B.L., and A.S. Gladfelter. 2021. The state of the septin cytoskeleton from assembly to function. *Curr. Opin. Cell Biol.* 68:105–112. https://doi.org/10.1016/j.ceb.2020.10.007

Ye, M., K.M. Lehigh, and D.D. Ginty. 2018. Multivesicular bodies mediate long-range retrograde NGF-TrkA signaling. *Elife.* 7:e33012. https://doi.org/10.7554/eLife.33012

Zheng, P., C.J. Obara, E. Szczesna, J. Nixon-Abell, K.K. Mahalingan, A. Roll-Mecak, J. Lippincott-Schwartz, and C. Blackstone. 2022. ER proteins decipher the tubulin code to regulate organelle distribution. *Nature.* 601:132–138. https://doi.org/10.1038/s41586-021-04204-9

Supplemental material

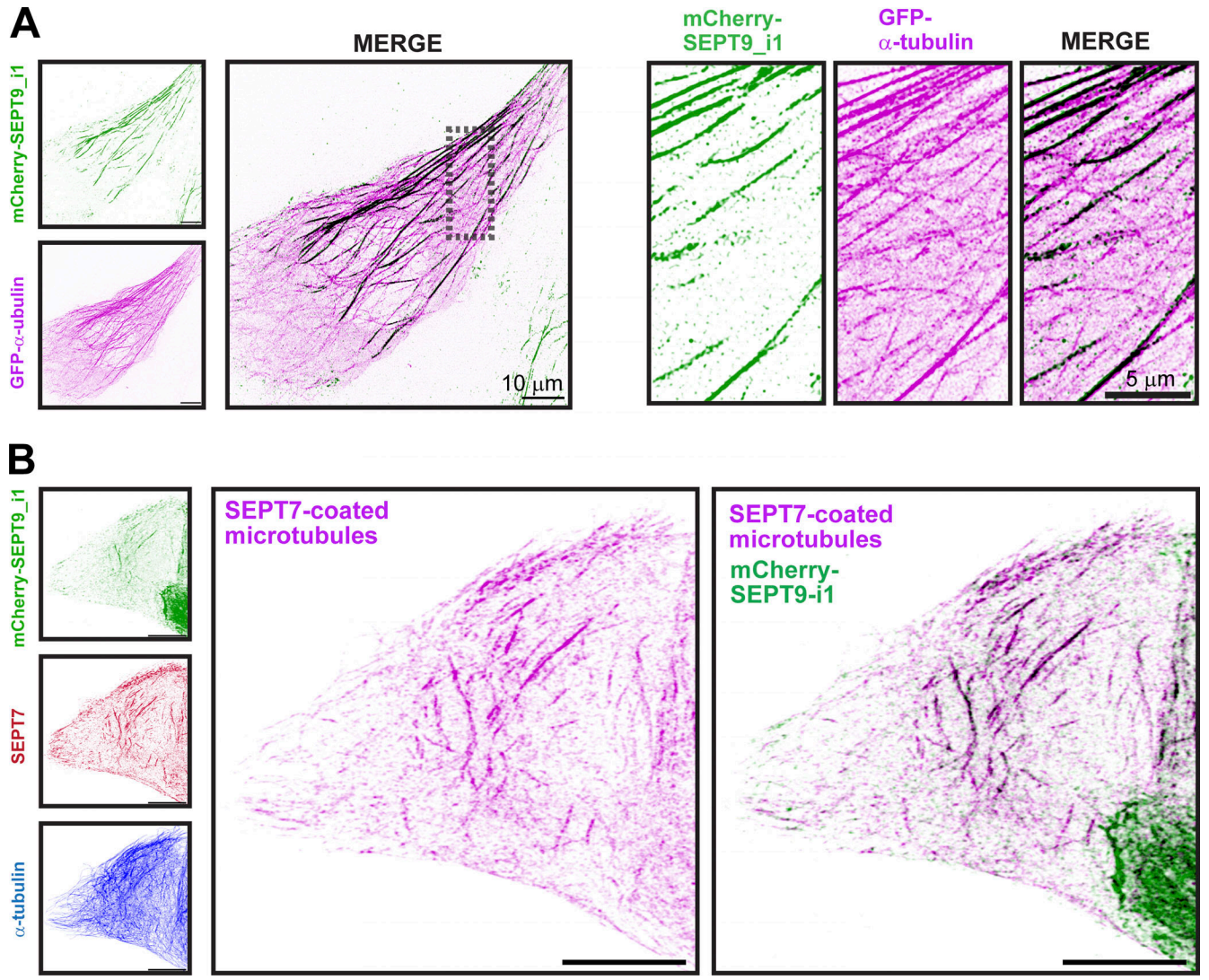

Figure S1. **Septins localize to a subset of microtubules in MDCK cells. (A)** Maximum intensity projection images of super-resolution confocal microscopy z-series stack of an MDCK cell expressing α-tubulin-GFP (inverted forest green) and mCherry-SEPT9_i1 (inverted magenta). Outlined region (dashed rectangle) is shown in higher magnification. Scale bars, 10 µm (low magnification) and 5 µm (high magnification). **(B)** Maximum intensity projection images of a super-resolution confocal microscopy z-series stack of an MDCK-mCherry-SEPT9_i1 cell, which was stained for endogenous α-tubulin and SEPT7. An artificial microtubule-SEPT7 overlap channel was created (SEPT7-coated microtubules), showing all α-tubulin fluorescence that colocalizes with SEPT7 (inverted magenta), and the overlay between this channel and mCherry-SEPT9_i1 (inverted forest green) is displayed. Scale bar, 10 µm.

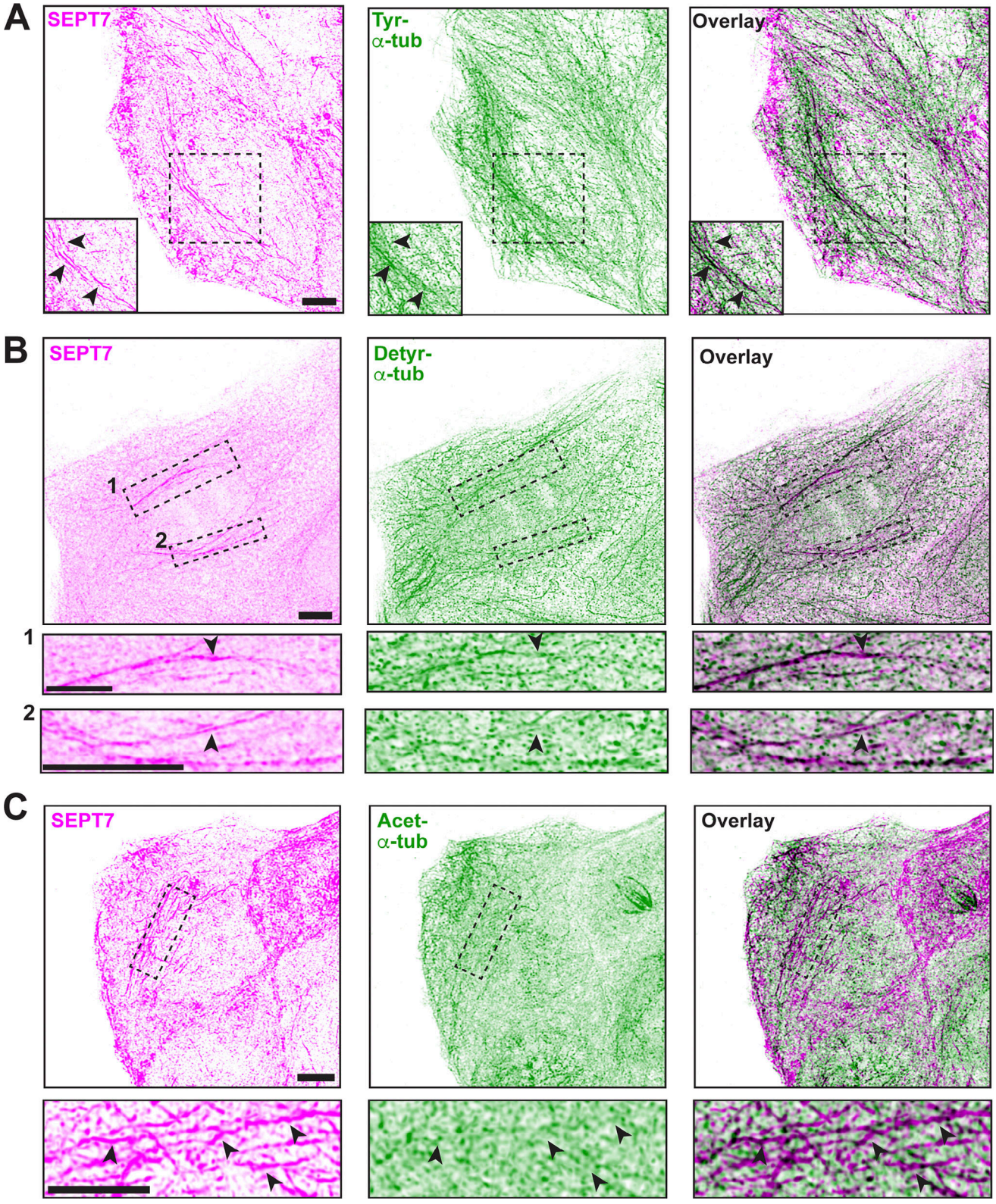

Figure S2. **Septin localization with respect to tyrosinated, detyrosinated, and acetylated microtubules. (A)** Maximum intensity projections of super-resolution confocal microscopy images of MDCK cells stained for endogenous SEPT7 and tyrosinated α-tubulin. Arrowheads point to SEPT7 colocalizing with tyrosinated microtubules. Scale bars, 5 µm. **(B)** Maximum intensity projections of super-resolution confocal microscopy images of MDCK cells stained for endogenous SEPT7 and detyrosinated α-tubulin. The outlined perinuclear regions 1 and 2 (dashed rectangle) are shown in higher magnification, and arrowheads point to SEPT7-coated microtubule segments with low levels of detyrosinated α-tubulin. Scale bars, 5 µm. **(C)** Maximum intensity projections of super-resolution confocal microscopy images of MDCK cells stained for endogenous SEPT7 and acetylated tubulin. The perinuclear region outlined with a dashed rectangle is shown in higher magnification, and arrowheads point to areas of SEPT7 enrichment with low levels of acetylated tubulin. Scale bars, 5 µm.

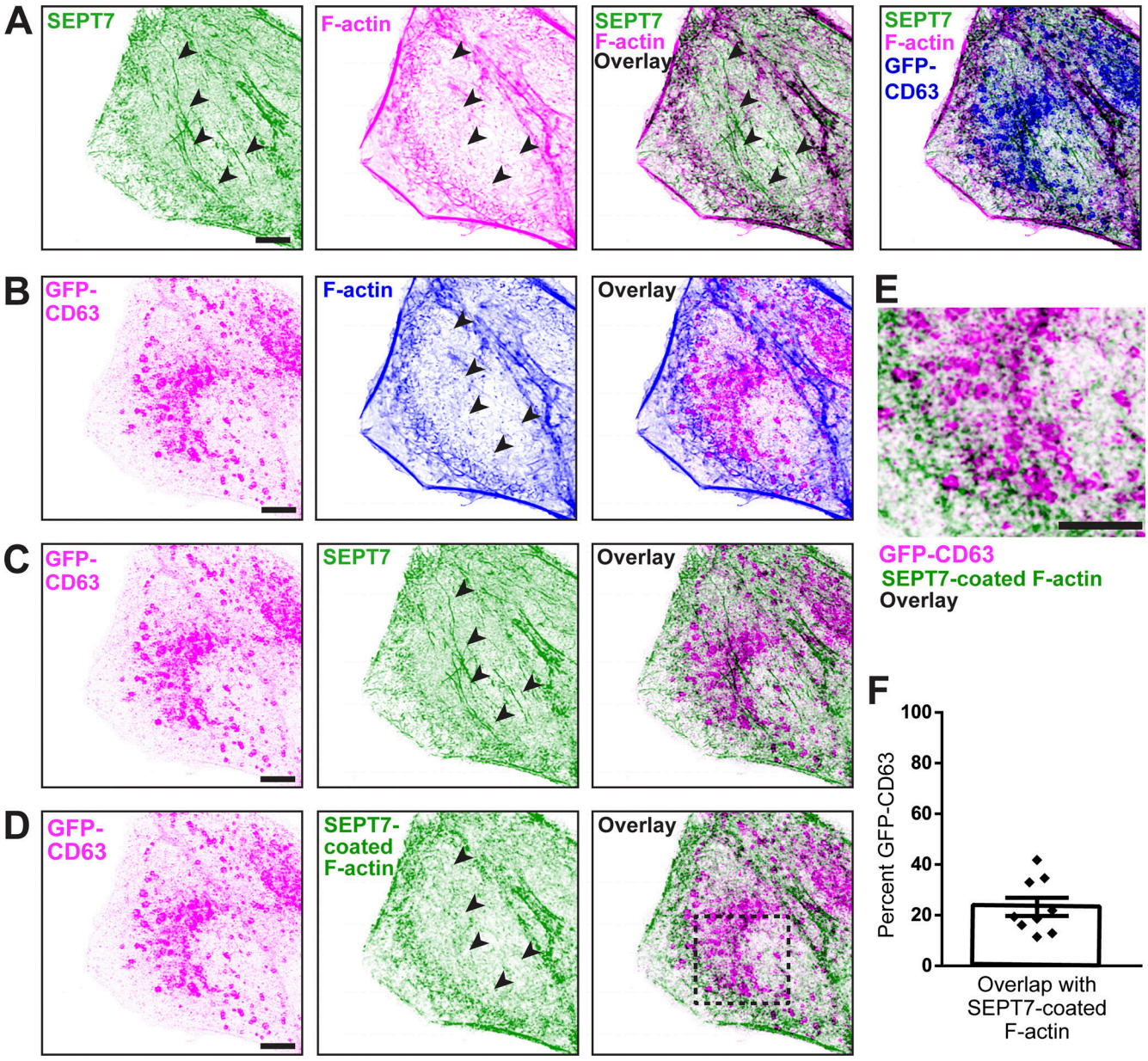

Figure S3. **Septin-coated actin filaments localize to the cellular periphery and have minimal overlap with GFP-CD63. (A)** Maximum intensity projections of super-resolution confocal microscopy images of MDCK cells stained for endogenous SEPT7 and actin in MDCK cells that express GFP-CD63. Arrowheads point to perinuclear septin filaments (SEPT7) that do not overlap with actin filaments. Scale bars, 5 µm. **(B and C)** Maximum intensity projections of super-resolution confocal microscopy images of the same MDCK (A) show the localization of GFP-CD63 with respect to actin (B) or SEPT7 (C). Arrowheads point to perinuclear septin filaments (SEPT7). Scale bars, 5 µm. **(D and E)** Maximum intensity projections of super-resolution confocal microscopy images of the same MDCK (A–C) show the localization of GFP-CD63 with respect to SEPT7-coated actin (D), a fluorescent channel that was artificially generated. The outlined perinuclear region of the merged image of GFP-CD63 and SEPT7-coated actin is shown in higher magnification (E). Arrowheads point to perinuclear septin filaments (SEPT7). Scale bars, 5 µm. **(F)** Bar graph shows the mean (±SEM, error bars) percentage of GFP-CD63 particles that overlap with septin-coated actin filaments (n = 9 cells).

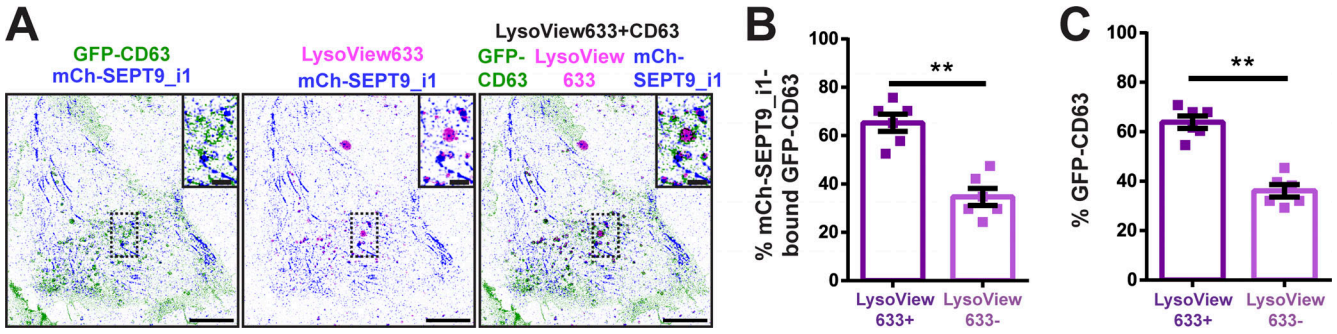

Figure S4. **Septin-bound GFP-CD63 endosomes are mainly acidic. (A)** Confocal microscopy image of a live MDCK cell that expresses mCherry-SEPT9_i1 (inverted blue) and GFP-CD63 (inverted forest green) after incubation with LysoView633 (inverted magenta). Outlined regions are shown in higher magnification. Scale bars, 10 and 2 µm (insets). **(B)** Quantification of the mean percentage (±SEM, error bars) of septin (mCherry-SEPT9_i1) bound GFP-CD63 endosomes with or without LysoView633 in subconfluent MDCK cells (n = 6). Data were statistically analyzed with a Mann-Whitney test. ** P < 0.01. **(C)** Quantification of the mean percentage (±SEM, error bars) of total GFP-CD63 endosomes with or without LysoView633 in subconfluent MDCK cells (n = 6). Data were statistically analyzed with a Mann-Whitney test. ** P < 0.01.

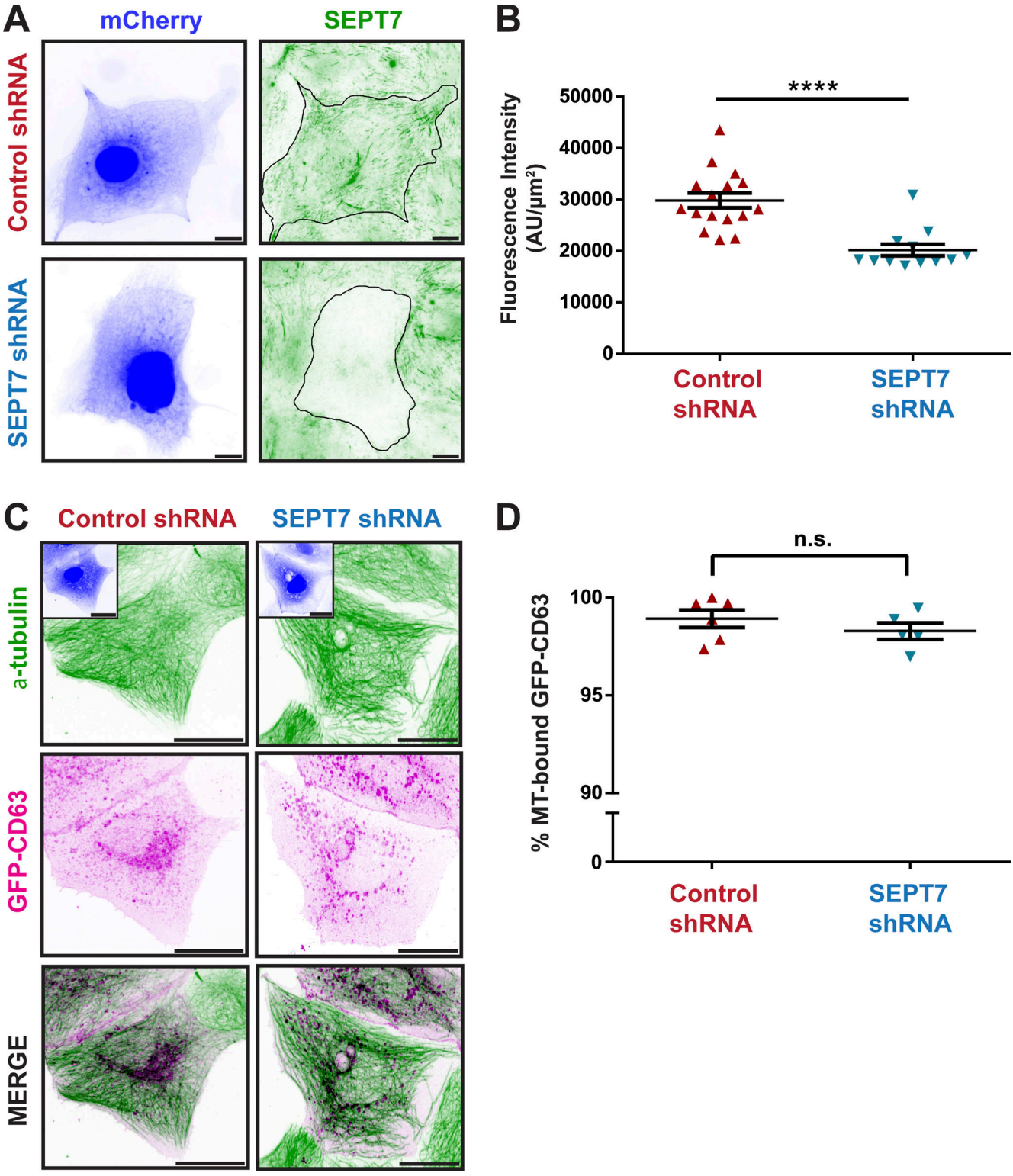

Figure S5. **SEPT7 knockdown abolishes septin filaments without disrupting GFP-CD63 association with microtubules. (A)** Widefield microscopy images of MDCK cells which were stained for endogenous SEPT7 (inverted forest green) after 48 h transfection with plasmids that express mCherry (inverted blue) and scramble control or SEPT7 shRNAs. Scale bars, 10 µm. **(B)** Mean (±SEM, error bars) SEPT7 fluorescence intensity per cell area after staining of MDCK cells (n = 6), which were transfected for 48 h with plasmids that express mCherry (inverted blue) and scramble control or SEPT7 shRNAs. Data were statistically analyzed with a Mann-Whitney test. **** $P < 0.0001$. **(C)** Maximum intensity projections of super-resolution confocal microscopy z-stack images of MDCK-GFP-CD63 cells (inverted magenta), which were stained for endogenous α-tubulin (inverted forest green) after 48 h transfection with plasmids that express mCherry (inverted blue) and scramble control or SEPT7 shRNAs. Scale bars, 10 µm. **(D)** Quantification of the mean percentage (±SEM, error bars) of GFP-CD63 endosomes that overlap with microtubules in MDCK cells (n = 6) after 48 h transfection with control and SEPT7 shRNAs. Data were statistically analyzed with a Mann-Whitney test. n.s., not significant.

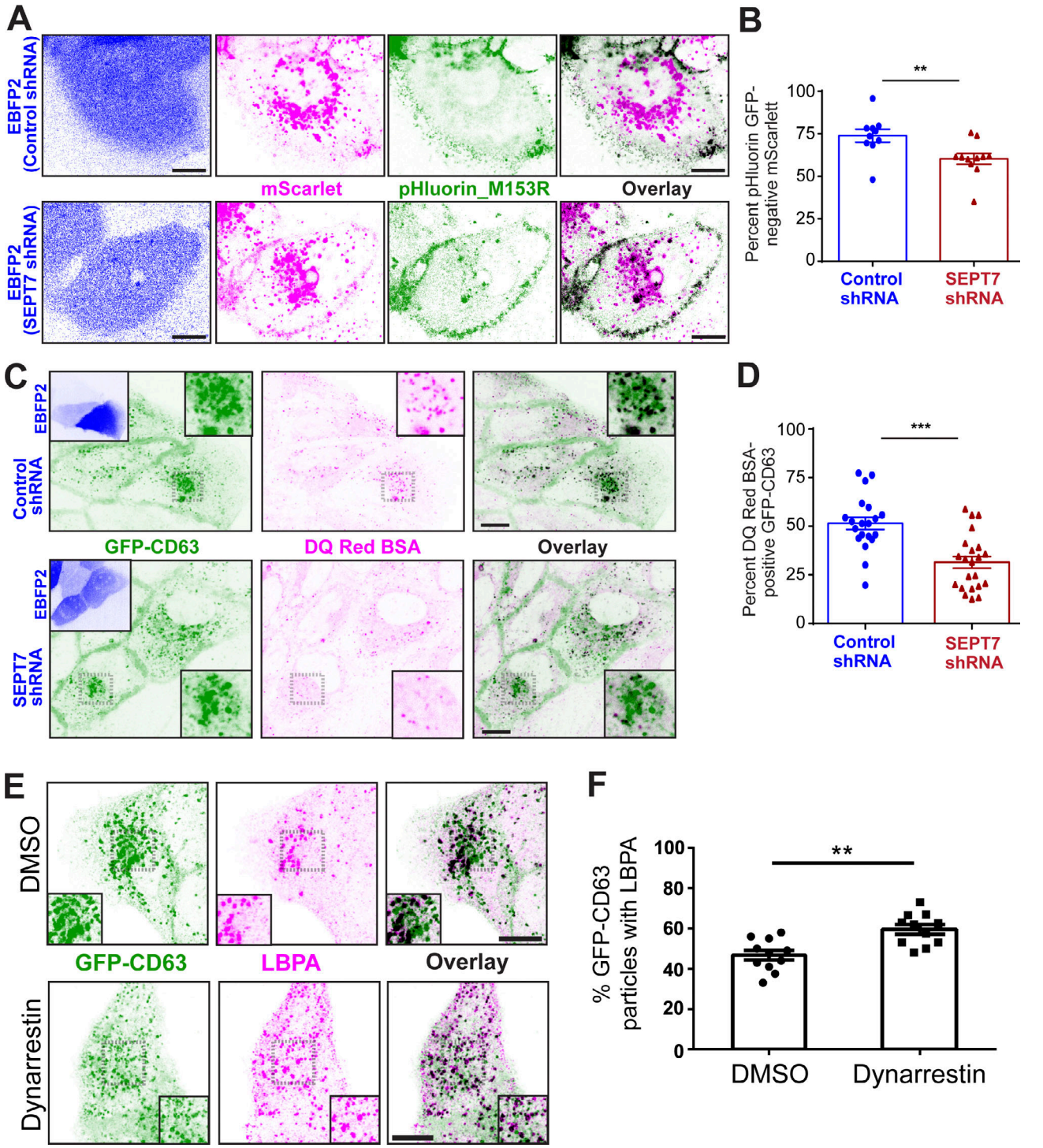

Figure S6. **Septin depletion reduces acidification of GFP-CD63 endosomes, and inhibition of dynein motility enhances the percentage of LBPA-positive GFP-CD63. (A)** Confocal microscopy sections of living MDCK cells after 36 h of transfection with pHluorin_M153R-CD63-mScarlet and scramble control or SEPT7 shRNA from EBFP2-expressing plasmid DNA. Scale bars, 10 µm. **(B)** Bar graph shows the mean (±SEM, error bars) percentage of mScarlet-labeled compartments that were free of GFP fluorescence per cell (n = 10–11). Data were analyzed with a Mann–Whitney U test ($P < 0.01$) and are representative of two independent experiments. **(C)** Spinning disk confocal microscopy images of living MDCK-GFP-CD63 cells imaged after 6 h of incubation with DQ Red BSA, which followed a 36-h transfection with plasmids co-expressing EBFP2 and control or SEPT7 shRNA. Scale bars, 10 µm (main panels, EBFP2 insets) and 5 µm (insets of outlined regions). **(D)** Bar graph shows the mean percentage (±SEM, error bars) of GFP-CD63 compartments that contained DQ Red BSA per cell (n = 20–22). Data were analyzed with a Mann–Whitney U test ($P < 0.001$) and are representative of two independent experiments. **(E)** Confocal microscopy sections of MDCK-GFP-CD63 cells, which were stained with an antibody against LBPA after 30 min of treatment with carrier (DMSO) or dynarrestin (10 µM). Insets show outlined regions of the perinuclear cytoplasm in higher magnification. Scale bars, 10 and 5 µm (insets). **(F)** Bar graph shows the mean percentage (± SEM, error bars) of GFP-CD63 endosomes that contain LBPA per cell (n = 11). Data were analyzed with an unpaired t test ($P = 0.001$) and are representative of two independent experiments. ** $P < 0.01$, *** $P < 0.001$.

Video 1. **Examples of immotile GFP-CD63 endosomes on mCherry-SEPT9_i1 filaments.** Time-lapse super-resolution spinning disk confocal microscopy of an MDCK cell expressing mCherry-SEPT9_i1 (green) and GFP-CD63 (magenta). Video captured over the course of 3 min at 4 frames per second (fps). Playback is at 60 fps. Video stills are shown in Fig. 2 A. Scale bar, 1 µm.

Video 2. **Examples of GFP-CD63 endosomes switching between mCherry-SEPT9_i1 filaments.** Time-lapse super-resolution spinning disk confocal microscopy of an MDCK cell expressing mCherry-SEPT9_i1 (green) and GFP-CD63 (magenta). Video captured over the course of 2 min at 4 fps. Playback is at 60 fps. Video stills are shown in Fig. 2 B. Scale bar, 1 µm.

Video 3. **Example of processive GFP-CD63 movement along an mCherry-SEPT9_i1 filament.** Time-lapse super-resolution spinning disk confocal microscopy of an MDCK cell expressing mCherry-SEPT9_i1 (green) and GFP-CD63 (magenta). Arrowhead points to GFP-CD63 endosome moving processively along a septin filament. Video captured over the course of 18 s at 4 fps. Playback is at 20 fps. Video stills are shown in Fig. 2 D. Scale bar, 1 µm.

Video 4. **In vitro reconstitution of GFP-CD63 motility on uncoated microtubules.** Time-lapse TIRF microscopy of isolated GFP-CD63 containing endosomes (magenta) in cell-free in vitro assays with taxol-stabilized microtubules (green). Video captured over the course of 1 min at 2 fps. Playback is at 20 fps. Fig. 3 A shows a kymograph of GFP-CD63 movement from this video. Scale bar, 1 µm.

Video 5. **Example of GFP-CD63 pausing on microtubule-bound mCherry-SEPT2/6/7 in a cell-free in vitro reconstitution assay.** Time-lapse TIRF microscopy of isolated GFP-CD63 containing endosomes (magenta) in cell free in vitro assays with taxol-stabilized microtubules (green) coated with mCh-SEPT2/6/7 (cyan). Video captured over the course of 1 min at 2 fps. Playback is at 20 fps. Fig. 3 B shows a kymograph of GFP-CD63 movement and pausing. Scale bar, 1 µm.

Video 6. **Example of GFP-CD63 immobilization on mCherry-SEPT2/6/7/9-coated microtubules in a cell-free in vitro reconstitution assay.** Time-lapse TIRF microscopy of isolated GFP-CD63 containing endosomes (magenta) in cell free in vitro assays with taxol-stabilized microtubules coated with mCh-SEPT2/6/7/9 (cyan). Video captured over the course of 1 min at 2 fps. Playback is at 20 fps. Fig. 3 C shows a kymograph from this video. Scale bar, 1 µm.

Video 7. **Representative example of GFP-CD63 trafficking in an MDCK cell transfected with control scrambled shRNA.** Time-lapse super-resolution spinning disk confocal microscopy of a live MDCK cell that expresses GFP-CD63 (gray) and is transfected with a SCRMBL control shRNA. Trajectories show the cumulative movement of motile GFP-CD63 compartments in the cellular mid-zone over the course of the previous 30 frames; trajectories are color-coded in shades of fading red to denote movements with higher (bright red) and lower (light pink) velocities. Video captured over the course of 90 s at 5 fps. Playback is at 40 fps. Fig. 6 A shows frames with trajectories of cumulative GFP-CD63 movement from this video. Scale bar, 10 µm.

Video 8. **Representative example of enhanced GFP-CD63 movement in an MDCK cell transfected with SEPT7 shRNA.** Time-lapse super-resolution spinning disk confocal microscopy of a live MDCK-GFP-CD63 cell that was transfected with SEPT7 shRNA. Trajectories show the cumulative movement of motile GFP-CD63 compartments in the cellular mid-zone over the course of 60 frames; trajectories are color-coded in shades of fading red to denote movements with higher (bright red) and lower (light pink) velocities. Video captured over the course of 90 s at 5 fps. Playback is at 40 fps. Fig. 6 B shows frames with trajectories of cumulative movement from this video. Scale bar, 10 µm.